Title

Specific populations of basal ganglia output neurons target distinct brain stem areas while collateralizing throughout the diencephalon

Permalink

https://escholarship.org/uc/item/17k086j9

Journal

Neuron, 109(10)

ISSN

0896-6273

Authors

McElvain, Lauren E
Chen, Yuncong
Moore, Jeffrey D
et al.

Publication Date

2021-05-01

DOI

10.1016/j.neuron.2021.03.017

Peer reviewed

Published in final edited form as:

Neuron. 2021 May 19; 109(10): 1721–1738.e4. doi:10.1016/j.neuron.2021.03.017.

Specific populations of basal ganglia output neurons target functionally distinct brainstem areas while collateralizing throughout the diencephalon

Lauren E. McElvain[1,2,3], **Yuncong Chen**[4,7], **Jeffrey D. Moore**[5,7], **G. Stefano Brigidi**[2], **Brenda L. Bloodgood**[2], **Byung Kook Lim**[2], **Rui M. Costa**[3,6,*], **David Kleinfeld**[1,2,8,*]

[1]Department of Physics, University of California San Diego, La Jolla, CA 92093, USA

[2]Section of Neurobiology, University of California at San Diego, La Jolla, CA 92093, USA

[3]Champalimaud Neuroscience Programme, Champalimaud Centre for the Unknown, Lisbon, 1400-038, Portugal

[4]Department of Computer Science, University of California San Diego, La Jolla, CA 92093, USA

[5]Department of Molecular and Cell Biology, Harvard University, Cambridge, MA 02138, USA

[6]Zuckerman Institute and Department of Neuroscience, Columbia University, New York 10027 USA

[7]These authors contributed equally

[8]Lead contact

Abstract

The basal ganglia play a central role in regulating behavior, yet the organization of their outputs to other brain areas is incompletely understood. We investigate the largest output nucleus, the substantia nigra pars reticulata (SNr), and delineate the organization and physiology of its projection populations in mice. Using genetically-targeted viral tracing and whole-brain anatomical analysis, we identify over forty SNr targets, which encompass a roughly 50-fold range of axonal densities. Retrograde tracing from the volumetrically largest targets indicates that SNr contains segregated subpopulations that differentially project to functionally distinct brainstem regions. These subpopulations are electrophysiologically specialized, topographically organized, and collateralize to common diencephalon targets, including motor and intralaminar thalamus, as well as the pedunculopontine nucleus and the midbrain reticular formation. These findings

---

[*]Correspondence: dk@physics.ucsd.edu (DK), rc3031@columbia.edu (RMC).

Author Contributions

R.M.C., D.K., B.K.L. and L.E.M., conceived the study and designed the experiments, L.E.M. conducted anatomical and electrophysiological experiments. G.S.B. performed in situ hybridization experiments. Y.C., D.K., L.E.M. and J.D.M. formulated analysis tools. L.E.M. analyzed data. B.L.B., R.M.C., and D.K. supplied reagents, and R.M.C., D.K. and L.E.M. wrote the manuscript.

Declaration of Interests

The authors declare no competing interests.

establish that SNr signaling is organized as dense, parallel outputs to specific brainstem targets, concurrent with extensive collateral branches that encompass the majority of SNr axonal boutons.

eTOC Blurb for McElvain et al.

McElvain et al. map the complete set of brain-wide projections from the largest output nucleus of the murine basal ganglia, the substantia nigra pars reticulata. Spatially segregated and electrophysiologically distinct subpopulations are revealed that project to different brainstem regions, along with extensive collaterals to the pedunculopontine nucleus and diencephalon targets.

Graphical Abstract

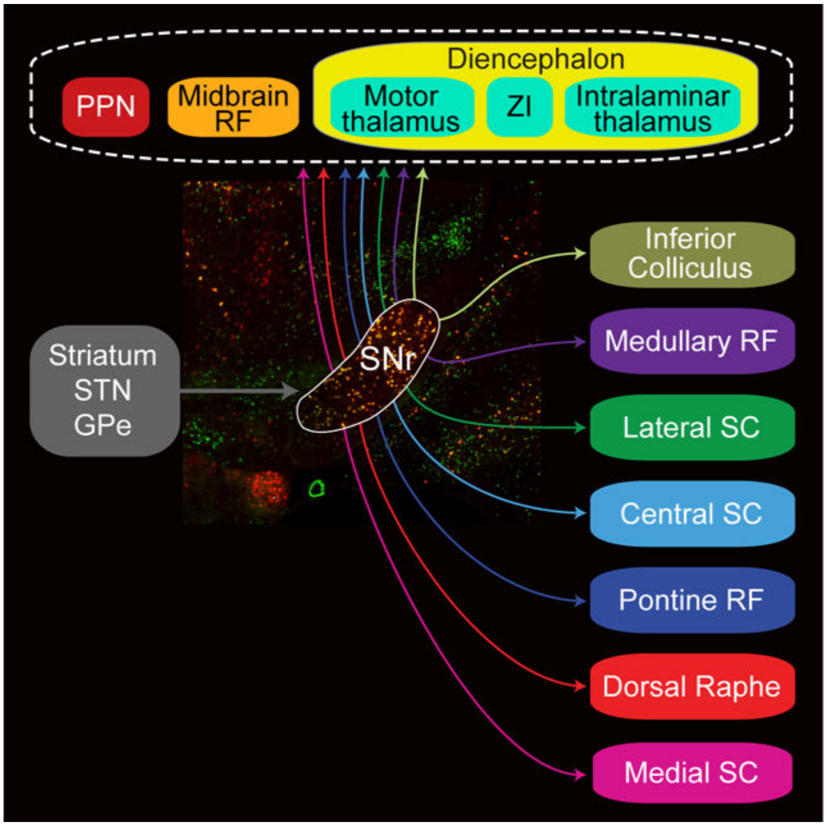

INTRODUCTION

Motor actions are the consequence of neuronal computations in circuits that are distributed broadly across the nervous system (Grillner, 2006; Kuypers, 1981; Towe and Luschei, 2013). Individual components of the motor system have been studied extensively, with prominent attention given to the cerebral cortex, basal ganglia, and cerebellum. These studies have yielded deep insights into local signaling within each structure (Klaus et al., 2019; Peters et al., 2017; Raymond and Medina, 2018). However, the organization and circuit mechanisms that connect nodes of the motor system to each other remain largely unknown.

Here we investigate the circuit basis by which outputs of the basal ganglia impinge on the broader motor system. The basal ganglia form an essential component of the volitional motor system and mediate fundamental aspects of behavioral regulation and learning (Alexander et al., 1990; Hikosaka et al., 2014; Jin and Costa, 2015; Turner and Desmurget, 2010). Disruption to the basal ganglia network underlies common movement disorders, including Parkinson's disease and Tourette Syndrome (Mink, 2001; Nelson and Kreitzer, 2014) and impairs control of the limbs, trunk, facial, oral, and vocal musculature (DeLong, 2011; Robbins et al., 1986; Visser and Bloem, 2005). Moreover, basal ganglia dysfunction has also been implicated in cognitive and affective control. Despite this broad behavioral importance, the basis by which the basal ganglia outputs connect to downstream networks to mediate such diverse functions is poorly understood.

Neurons in the volumetrically largest output nucleus of the basal ganglia, the substantia nigra pars reticulata (SNr), emit well-established projections the superior colliculus, motor and intralaminar thalamic nuclei, and the pedunculopontine nucleus (PPN) (Alexander et al., 1990; Hikosaka, 2007b; Mena-Segovia et al., 2004). However, the extent to which projections to well-established targets arise from the same or segregated neurons is debated (Anderson and Yoshida, 1977; Beckstead and Frankfurter, 1982; Deniau et al., 1977; Parent et al., 1983). SNr neurons exhibit heterogeneous firing responses during behavior (DeLong et al., 1983; Gulley et al., 2002; Hikosaka and Wurtz, 1983; Jin and Costa, 2010), suggesting the nucleus might contain functionally distinct projection types. Moreover, evidence from past studies indicates SNr projects to additional domains of the brainstem and diencephalon (Cebrian et al., 2005; Chronister et al., 1988; Gervasoni et al., 2000; Pollak Dorocic et al., 2014; Schneider et al., 1985; Takakusaki et al., 2003; Von Krosigk and Smith, 1991; Yasui et al., 1992). The lack of systematic circuit mapping has hindered a comprehensive identification of SNr target regions, and, furthermore, it remains unknown whether SNr contains distinct classes of projection neurons.

To delineate the circuit logic of basal ganglia output signaling and projection cell types in SNr, we first address the mesoscopic organization of SNr projections and determine the electrophysiological properties of SNr neurons. We ask: (1) Which brain regions are the major targets of SNr axonal projections? (2) Do different electrophysiological properties of SNr cells correspond to distinct output populations? (3) Do neurons in the SNr project equally to all major targets, as expected for a global hub-like architecture (Figure 1A)? Or rather, does SNr contain segregated projection populations that preferentially project to different targets (Figure 1B)? To address these questions, we combine state-of-the-art viral circuit mapping, high-resolution whole-brain optical scanning, and electrophysiological recordings of identified projection neurons.

RESULTS

SNr Projects Broadly to Diverse Brainstem and Thalamic Regions

To identify the brain regions targeted by basal ganglia outputs, we mapped SNr axonal projections and synaptic terminals across the brain using genetically restricted viral tracing. The predominant population of neurons in SNr is parvalbumin-positive GABAergic neurons (Gonzalez-Hernandez and Rodriguez, 2000). We verified that 86.9 ± 1.0 % of GABAergic

SNr neurons express parvalbumin (14,901 neurons, 39 sections, 4 mice) (Figures 1C and S1A-C) throughout the rostral-caudal extent of the nucleus (Figures S1B). To label the axons and presynaptic boutons arising from this population, membrane-bound green fluorescent protein (mGFP) and synaptophysin-mRuby were virally expressed (AAV-DJ hSyn-FLEX-mGFP-2A-Synaptophysin-mRuby) in SNr neurons in Parvalbumin-Cre (PV-Cre) mice (Figure 1D). High-resolution, whole-brain slide scanning of SNr projections reveals axon terminations that extend over seven millimeters, from anterior thalamus to the caudal brainstem (Figure 1E–1L).

In the diencephalon, SNr targets include major motor (VM and VA) and intralaminar/midline (MD, CL/CM, and Pf) thalamic nuclei (Figures 1E–1G), as in other species (Cebrian et al., 2005; Graybiel and Ragsdale, 1979; Utter and Basso, 2008), as well as the thalamic reticular nucleus, zona incerta, fields of Forel, and prerubral field (Figure S2A-S2G). A greater number of targets are observed in the brainstem. Beyond well-established projections to the superior colliculus and PPN (Hikosaka, 2007b) (Figures 1H and 1I), extensive SNr projections target volumetrically large domains of the reticular formation in the midbrain (MidRF), pons (PNo), and medulla (Med, subdivisions PcRT and IRT), as well as 17 small premotor nuclei (Figures 1H–1K, S2H-SK, and S3). Downstream brainstem targets span regions that have been implicated in oculomotor and head orientation (superior colliculus, INC/MA3/Su3) (Fukushima, 1987; May et al., 2019), orofacial sensorimotor systems (Med, Su5, P5, and L5) (Kolta et al., 2010; McElvain et al., 2018), hindlimb control (PNo) (Brownstone and Chopek, 2018), neuromodulation (PPN and DR), and nuclei implicated in heterogeneous or unknown functions, i.e., the precuneiform nucleus, red nucleus, subdivisions of the periaqueductal grey and parabrachial nuclei (Figures S2 and S3). All together, we identified significant SNr projections to 42 distinct regions (Figure 2A).

GABAergic neurons throughout the extent of SNr express parvalbumin (Figures 1C and S1) and GAD2 mRNA (Figure S1C), with large neurons in dorsolateral SNr highly expressing parvalbumin and smaller neurons in ventromedial SNr expressing lower levels (Figure S1A) (Gonzalez-Hernandez et al., 2001; Gonzalez-Hernandez and Rodriguez, 2000). To test whether the smaller percentage of parvalbumin-negative SNr GABAergic neurons project to distinct downstream targets, we performed additional axonal tracings from SNr in VGAT-Cre mice (Figures S2 and S3). Whole-brain analysis revealed a comparable projection pattern from SNr in VGAT-Cre and PV-Cre mice (Figures S2L and S2M).

Across the 42 downstream targets of SNr in the diencephalon and brainstem, the density of SNr bouton innervation spans a continuous range over more than one and a half orders of magnitude (Figure 2A, left). When we account for the volume of downstream structures (Figure 2A, middle), the total SNr bouton output is enriched in a limited set of structures, including VM thalamus, PPN, and the dorsal zona incerta, i.e., 6.1 %, 5.8 %, and 4.6 % of total SNr output, respectively. Nearly two-thirds of output from the SNr targets the brainstem reticular formations and the colliculi (33.9% across Mid, PNo, PcRT/IRT and 30.9 % across CSC, LSC, MSC, and IC), while the remaining 32 structures each contribute < 2 % of total bouton output (Figures 2A, right and 2D).

A quantitative analysis shows that the probability density function for the axonal density is roughly exponentially distributed across the major fraction of SNr targets until a plateau is reached (black scale, Figure 2B). The plateau corresponds to the innervation of the densest targets. These targets comprise the well-established SNr targets, i.e., VA and VM motor thalamus, PPN, and the superior colliculus (Figures 2B and 2C), however a vast majority of total SNr output spans areas outside of these targets (Figure 2D). Taken together, SNr targets an expansive and diverse set of anatomical substrates (Figures 2A, S2, and S3) through a continuum of dense-to-sparse projections (Figures 2A-C). The major fraction of total output is concentrated in several large brainstem regions and, to a lesser extent, the zona incerta and motor thalamus (Figure 2D).

SNr Neurons Exhibit Heterogeneous Electrophysiological Properties

Do SNr neurons have diverse intrinsic electrophysiological properties? The spiking responses of SNr neurons during behavior include both increases and decreases in rate across broad ranges and variable durations (Atherton and Bevan, 2005; Gulley et al., 1999; Hikosaka and Wurtz, 1983; Jin and Costa, 2010; Richards et al., 1997). It is unknown whether this heterogeneity arises from different synaptic inputs, either through afferents or network interactions, or a spectrum of electrophysiological properties intrinsic to SNr neurons. To assess the firing properties across SNr neurons, we first performed whole-cell patch-clamp recordings from SNr neurons in young-adult mouse midbrain slices. Across the population, neurons (120 cells from 14 mice) exhibited a capacity for highly regular and tonic firing (Figure 3A), rapid action potential kinetics (Figure 3B), and sustained, high-rate activity (Figure 3C). Most critical, SNr firing responses to depolarizing inputs are highly linear ($R^2 = 0.99 \pm 0.01$) (Figure 3C). The limited adaptation and linearity of the neuronal input-output relation is consistent with open-loop drive for a motor system (Åström and Murray, 2008), akin to linear neuronal and synaptic properties common in brainstem sensorimotor networks (Kolkman et al., 2011; McElvain et al., 2010) and unlike forebrain projection neurons. In contrast, responses to hyperpolarizing inputs are non-linear, and the capacity for post-inhibitory rebound firing varied significantly across the population (Figure 3D). The broad continuum found for each electrophysiological property, e.g., gain, firing rate ranges, and rebound kinetics, can differentially tune the firing capabilities of individual neurons in SNr.

Distinct SNr Subpopulations Project to Large Brainstem Effector Regions

We next ascertained how the remarkable diversity of SNr cellular properties maps onto specific anatomical projection targets. The large brainstem targets of SNr have been implicated in disparate behavioral functions, involving distinct body parts and muscle groups. Do distinct SNr neuron pools that project to different downstream effector regions have specialized electrophysiological properties? To test this possibility, we first injected each of the large brainstem regions (Figure 2A, middle) with a fluorescent retrograde tracer and targeted whole-cell recordings to labeled projection neurons (Figure 4A). In the hindbrain, the large SNr targets are the medullary reticular formation (Med, i.e., subdivisions PcRT/IRT), pontine reticular formation (PNo), and the dorsal raphe (DR) (Figure 1I–1K). Large midbrain targets of SNr are the inferior (IC) and superior colliculi (SC) (Figures 1H). Three medial-lateral domains of SC were treated separately in light of the spatial specificity of their visual and somatosensory inputs (Comoli et al., 2012; Drager and Hubel, 1976) and topographical organization of collicular output projections from the lateral superior colliculus (LSC), central superior colliculus (CSC), and medial superior colliculus (MSC) (Dean et al., 1988; Redgrave et al., 1987a, b; Wang and Redgrave, 1997; Yasui et al., 1994) (Figure S4).

We find that SNr neurons projecting to different large brainstem regions exhibit notable electrophysiological specializations (4–7 mice per each target; see Figure S5 for injection parameters). Projections to the colliculi arise from neuronal pools with different signaling capabilities. Neurons that project to the lateral and central superior colliculus have a relative rapid rise and fall to their action potential, as seen by plotting the derivative, dV/dt, versus the amplitude of the transmembrane potential, V (Figure 4B, left blue and green curves), and high spontaneous and maximum firing ranges (Figures 4C–4D). In contrast, projections to medial superior and inferior colliculus arise from relatively slower neuronal pools (Figures 4B–4D). SNr projections to hindbrain targets exhibit electrophysiological differences such that projections to the reticular formations, PNo and Med, exhibit rapid rise and fall to their action potential and high spike rates (Figures 4B–4D). In contrast, neurons projecting to the dorsal raphe exhibit slow action potentials, low firing rates, long time constants, and comprise the slowest projection population in SNr (Figures 4B–4D). Rather than spanning the full diversity in SNr, the intrinsic parameters of each of these projection populations span a restricted range (Figures 4D, S5C, and S6). This shows that different projection populations have specific functional properties.

Neurons in the SNr that project to brainstem areas span a range of post-inhibitory rebound firing capabilities. Robust non-linear rebound firing responses to hyperpolarization are greatest in neurons projecting to the medullary reticular formation and the inferior colliculus, which exhibited bursting up to 100 s of spikes/s and averaged 69 ± 15 Hz and 58 ± 11 Hz, respectively (Figure 4E). In contrast, transient and sustained rebound firing of other projection populations is modest and neurons projecting to the dorsal raphe exhibit the lowest capacity for rebound (Figures 4E). Thus, rather than each projection population spanning the full continuum of electrophysiological properties, projections to large brainstem areas arise from subpopulations of SNr neurons whose properties are differentially tuned.

SNr-brainstem projection neurons spatially cluster within the SNr (Figure 4F) and form a spatial continuum of electrophysiological properties (Figure S6C). Projection neurons that exhibit slower active and passive properties are concentrated in the medial portion of the nucleus (Figure S6C), which overlaps with terminal fields from associative striatal regions. Slow neurons are additionally located in a small cluster at the dorsal-most extreme portion of SNr, which extends in the substantia nigra, lateralis (SNl) and overlaps with terminal fields from auditory striatum (Deniau et al., 1996) (Figure 4F). In contrast, rapidly-responding projection neurons occupy the lateral half of SNr (Figures 4F and S6), where sensorimotor striatal afferents terminate (Deniau et al., 1996), thereby positioning different SNr projection neurons to differentially process striatal signals.

Broadly Tuned SNr Projections to Thalamic Nuclei and the Pedunculopontine Nucleus

We next targeted neurons that project to major thalamic nuclei and the pedunculopontine nucleus (PPN) (Figure 5) for whole-cell recordings. SNr neurons projecting to ventroanterior (VA), mediodorsal (MD), or parafascicular (Pf) thalamus each displayed the full diversity of firing properties observed across SNr neurons (Figures 5A–5C and S5C). Similarly, SNr neurons projecting to the PPN were broadly tuned with heterogeneous properties (Figures 5A–5C) and lacked statistically significant differences from randomly selected SNr neurons (Figure 5E). In addition to a lack of specialized intrinsic properties, SNr-thalamus and SNr-PPN projection neurons were distributed throughout SNr (Figure 5D). Taken together, SNr populations retrogradely labeled from several brainstem regions exhibit intrinsic electrophysiological properties that statistically differ from randomly targeted SNr neurons (Figure 5E), indicating each of these regions is dominated by output from a subpopulation of SNr neurons. In contrast, SNr populations labeled from the PPN and thalamic nuclei exhibit no highly significant differences (Figure 5E). To assess pairwise differences between populations, we additionally calculated the Euclidean distance between all z-scored intrinsic parameters and resampled the datasets to assess significance. The populations of SNr neuron projecting to brainstem targets extensively differed from each other, in contrast to SNr-thalamus and PPN projection neurons (Figure 5F). Thus, projections to thalamus and PPN arise from broadly tuned projection pools in SNr, in contrast to the specialized features of SNr projections to most large brainstem areas.

Collateral Organization of SNr Projections is Broad and Specific

The heterogeneity of SNr neurons that project to PPN and thalamic nuclei could arise from two possible circuit configurations. First, each of these projections could arise from a distinct, broadly tuned and spatially distributed population or, second, these projections could arise from converging collaterals of the diverse SNr projection populations that target large brainstem regions (Figure 4). Consistent with the second possibility, SNr neurons that project to PPN and thalamic nuclei exhibit topographical organization in their electrophysiological properties, such that thalamus-projecting neurons in lateral SNr are larger, fire at faster rates, and have faster membrane time constants (Figure S6), comparable to SNr neurons that project to large brainstem targets. The presence of collateral projections to the thalamus, superior colliculus, and PPN previously has been assayed with dual chemical tracer injection and antidromic stimulation, with conflicting results (Anderson and Yoshida, 1977; Beckstead and Frankfurter, 1982; Deniau et al., 1977; Parent et al., 1983). We utilized an intersectional virus mapping strategy to unambiguously determine the complete pattern of SNr collateralization (Figure 6A). To label collaterals throughout the brain, a rabies-pseudotyped lentivirus expressing Cre was injected into a single downstream target in each mouse. This virus retrogradely infected SNr projection populations, and a Cre-dependent AAV expressing eYFP (AAV2.2-Ef1a-DIO-eYFP) was targeted to SNr to label projection neurons and their terminals with eYFP (Figures 6B–6D). Whole-brain slide scanning was used to assess whether eYFP+ projection neurons emitted axonal collaterals in additional regions.

We injected the retrograde lentivirus into each of eight volumetrically large brainstem regions (Figure 6E, n = 18 mice). These encompass regions that receive a disproportionally large fraction of total SNr output (Figure 2D) and whose projection neurons from the SNr exhibit differing electrophysiological properties (Figure 4). From each population of SNr neurons projecting to large brainstem areas, axons collaterals were observed in diverse additional targets (Figures 6E and S7). SNr projection neurons retrogradely labeled from the dorsal raphe (DR), pontine reticular formation (PNo), medullary reticular formation (Med), lateral superior colliculus (LSC), central superior colliculus (CSC), and medial superior colliculus (MSC) each collateralize densely to diencephalic nuclei (labels in blue, Figure 6E; see also Figures S7 and S8), the PPN, and midbrain reticular formation (MidRF), but sparsely or not at all to each other. Additional collateral projections target a broad range of smaller brainstem sensorimotor nuclei (labels in gray, Figure 6E). As an exception, nigral projections to the inferior colliculus (IC), whose somata span dorsal SNr and SNl, do not collateralize extensively to the diencephalon, but do collateralize to the PPN, midbrain reticular formation (MidRF), and several premotor brainstem nuclei. The strength and probability of collaterals to diencephalic targets (Figure 6F) is more uniformly distributed than those to brainstem targets (Figure 6G). Lastly, on a statistical level, we see that the strength of collaterals is exponentially distributed over a 200-fold range (Figure 6H), on the same order-of-magnitude as seem in the initial anterograde mapping (Figure 2B). To verify that the PPN is indeed a broad collateral hub of SNr, the PPN was additionally targeted with the retrograde lentivirus. Consistent with data showing broad collaterals to the PPN, SNr neurons retrogradely labeled from the PPN collateralized to all other SNr targets (Figures 6E, top). Although SNr contains predominantly GABAergic neurons, a small population of dopaminergic neurons is also present SNr. (4.2 ± 0.1% of neuron in SNr tyrosine hydroxylase expressing, Figure S1)(Gonzalez-Hernandez and Rodriguez, 2000), and evidence suggests a fraction of putatively dopaminergic neurons in SNr project to thalamus and PPN (Cebrian and Prensa, 2010; Prensa and Parent, 2001). To verify that the collaterals mapped from SNr arise specifically from GABAergic neurons, we performed additional collateral tracing restricted to GABAergic SNr neurons. In particular, a Cre-dependent retrograde lentivirus that expresses Flp (RG-EIAV-DIO-FLP) was injected into a subset of downstream targets, and a Flp-dependent AAV (AAV2.2-fDIO-eYFP) was targeted to SNr in PV-Cre mice (Figure S7C). In this genetic- and projection-based intersectional tracing strategy, the eYFP+ collateral axons displayed a comparable pattern to those in wildtype mice, including collateral fibers in VM and Pf thalamus and the PPN (Figures S7D and S7E).

Together, these data indicate that SNr neurons emit broad but specific pattern of axonal collateralization, with diencephalic regions receiving broader collateral input than brainstem regions (Figure 6E–6G). This indicates that the SNr targets the diencephanon in a relatively diffuse manner compared to brainstem nuclei. In addition to diverse nuclei in the thalamus, two downstream brainstem targets also form common hubs for collateral inputs: the PPN and midbrain reticular formation. Notably, converging collaterals in common targets of SNr underlie their exceptionally dense bouton innervation (Figure 2C).

Parallel SNr Projections to Thalamus Exhibit Topographical Organization

The cerebral cortex and striatum contain highly organized subdomains (Gabbott et al., 2005; Nambu, 2011; Svoboda and Li, 2018), which questions how broad SNr collateralization to thalamic nuclei support behavioral or functional specificity within SNr-thalamo-cortical and SNr-thalamo-striatum feedback loops. Do ascending SNr projections fully intermix within thalamic nuclei, or alternatively, target specific nucleus subdomains? We performed automated reconstructions of SNr axon position in the diencephalon to ascertain fine-scale topography within thalamic nuclei. Serial sections of collateral axon locations were stacked and aligned to corresponding atlas sections (Franklin and Paxinos, 2013) and contour density computed relative to anatomical landmarks (Figure 7). Rather than spanning entire nuclei, axonal collateral fields of each SNr-brainstem projection pool target restricted subdomains. In both Pf and VM thalamus, collaterals from SNr-colliculus targeted relatively lateral domains of the nuclei (Figures 7A and 7B), whereas collateral projections SNr-hindbrain targeted relatively medial domains (Figures 7C and 7D).

To quantify the topography of SNr projections in thalamus, we measured the Euclidean distances between axonal terminal field centroids (Figure 7E). In Pf and VM thalamus, pairwise centroid distance measurements demonstrate that collateral axon fields of most populations were significantly offset (Figure 7E; $p < 0.01$) relative to the replicates within each population (Figures S8A and S8B). Topography was further assessed by measuring the extent of overlap between each collateral terminal field using the weighted Jaccard pairwise similarity index (Jaccard, 1912), denoted J_{AB} (Figure S8D), where $J_{AB} = 0$ indicates a lack of overlap and $J_{AB} = 1$ indicates complete overlap. Across Pf, VM, and VA motor thalamus, the Jaccard index of collateral overlap was small, i.e., 0.24 ± 0.12 (mean ± SD) and significant (Figures S8D and S8E). Thus, rather than intermixing, collateral projections from distinct SNr neuronal populations primarily tile the thalamic nuclei, comparable to the fine-scale topography of thalamic projections to cortex and striatum (Aldes, 1988; Cicirata et al., 1986; Mandelbaum et al., 2019; Smith et al., 2004), and consistent with segregated feedback loops.

The topography of SNr terminals in MD, CL/CM, and VA additionally shows spatial biases, although with a more complex pattern (Figure S8). Notably, while nigral projections to the inferior colliculus do not collateralize extensively to VM or Pf proper, spatial mapping of their axonal projections reveals sparse collateral projections to small domains on the periphery of VM and Pf (Figure S8A-S8C).

Topographically Organized Subdivisions of SNr

To assess the three-dimensional organization of projection pools within SNr, we reconstructed the positions of retrogradely labeled SNr projection neurons and aligned each experiment to a common reference frame (Figure 8A). Projection neuron populations are highly organized within SNr. Neurons projecting to the inferior colliculus (SNr-IC), medial superior colliculus (SNr-MSC), central superior colliculus (SNr-CSC), and lateral superior colliculus (SNr-LSC) are located relatively rostral and lateral of neurons projecting to the dorsal raphe (SNr-DR), PNo reticular formation (SNr-PNo), and medullary reticular formation (SNr-Med). Thus, SNr neurons that project to the colliculus spatially segregate from those that project to the hindbrain along a rostral-caudal division. Among SNr-colliculus neurons, those projecting to the inferior colliculus are most lateral/dorsal, while projections along the medial-to-lateral axis of the superior colliculus arise from neurons spanning the medial-to-lateral extent of rostral SNr. Along SNr-hindbrain neurons, SNr-DR, SNr-PNo, and SNr-Med neurons are situated along a medial-to-lateral axis in caudal SNr. Taken together, in addition to their topographically organized axon project patterns, projection neurons in SNr are positioned to operate as parallel, separable output modules.

DISCUSSION

This study demonstrates direct and extensive connections from the basal ganglia to diverse components of the thalamocortical and brainstem motor systems. Rather than a single monolithic output, SNr contains distinct projection neuronal pools that are electrophysiologically specialized, topographically organized, and differentially target brainstem effector circuits. Each projection pool emits ascending, spatially organized collateral branches to several thalamic nuclei and broadly collateralized to the pendunculopontine nucleus and midbrain reticular formation. These finding demonstrate that the well-known closed-loop architecture of basal ganglia-thalamo-cortical circuits overlaps with broad descending projections to brainstem premotor and modulatory networks. Taken together, this work establishes a framework of basal ganglia output via discrete SNr modules and their connections to the broader motor system.

Pattern of Mesoscopic Connectivity

Our anterograde tracing and analysis demonstrate that neurons in the SNr project to an unexpectedly large number of targets. The broad distribution of axonal density to collateral regions demonstrates that basal ganglia outputs are not organized in either as a one-to-all (Figure 1A) or a one-to-one (Figure 1B) circuit architecture. Rather, output projections arise from separable pools of neurons that broadcast to a discrete set of targets in the brainstem (Figure 4). These targets are large volumetric regions, i.e., central (CSC), medial (MSC), and lateral (LSC) domains of the superior colliculus, the inferior colliculus (IC), the dorsal raphe (DR), and pontine (PNo) and medullary (Med) reticular formations (Figure 2A). Each SNr projection pool sends a copy of their output to a set of common collateral targets that include the pedunculopontine nucleus (PPN) and midbrain reticular formation (MidRF) in the brainstem and the motor and intralaminar/midline thalamus and ZI in the diencephalon (Figures 6E and 8B). Importantly, whether every neuron in each projection pool follows the mesoscopic pattern or, alternatively, targets a further restricted set of targets remains to be determined.

Circuit Architecture: Descending and Ascending Connections to Broader Motor System

Axonal projections from SNr to large domains of the reticular formation and premotor nuclei throughout the midbrain, pons, and hindbrain (Figures 2, S2, and S3) reveal that the basal ganglia have extensive and relatively direct access to low-level motor circuitry. SNr targets many regions that project directly to the spinal cord, including the fields of Forel, zona incerta, medial parafascicular thalamic nucleus, red nucleus, interstitial nucleus of Cajal, superior colliculus, PPN, PAG, precuneiform nucleus, parabrachial nuclei, and distinct regions of the reticular formation (Liang et al., 2011); many SNr target regions additionally contain premotor neurons for orofacial, vocal, and oculomotor nuclei (Buttner-Ennever, 2006; Jurgens, 2002; McElvain et al., 2018; Stanek et al., 2014). Nearly all brainstem regions downstream of the SNr (Figures 2, S2, and S3) additionally receive afferents from the cerebral cortex (Alloway et al., 2010; Jeong et al., 2016; Sesack et al., 1989), as well as the cerebellum, hypothalamus, and amygdala (Asanuma et al., 1983; Holstege, 1987; Hopkins and Holstege, 1978). Identifying the mechanisms by which brainstem motor circuits integrate higher-order signals will be essential to understanding circuit basis of volitional movement and the consequences of output from the basal ganglia (Arber and Costa, 2018; Chen et al., 2019).

Theories of basal ganglia function largely have emphasized thalamocortical feedback loops and the role of the cerebral cortex in mediating basal ganglia effects on motor preparation and control (Alexander et al., 1990; Haber and Calzavara, 2009). In contrast, several lines of evidence have focused on SNr projections to a limited number of brainstem targets, particularly the role of SNr neurons that project to the superior colliculus (Hikosaka, 2007a; Holmes et al., 2012; Rossi et al., 2016; Wang and Redgrave, 1997). However, findings that SNr axons branch across several thalamic nuclei (Cebrian et al., 2005) and that these SNr-thalamus projections comprise aggregate collaterals of SNr-brainstem projection neurons (Figures 6, 7, and S8) establishes a principle of circuit organization by which SNr neurons concomitantly affect cortical and subcortical systems. Branching ascending-descending collateral projections might ensure coordinated gating of cortical and subcortical circuitry and are a practical consideration for the interpretations of experiments in which SNr neurons are retrogradely labeled from a single target. Similar ascending-descending branched projections have been observed among the outputs of diverse structures that regulate behavior, including the hypothalamus, cerebellum, and brainstem reticular formations (Bentivoglio and Kuypers, 1982; Risold et al., 1997; Schiebel, 2011).

Topographical Organization of Basal Ganglia Connectivity

The basal ganglia exhibit topographically organized inputs to the striatum (Hintiryan et al., 2016; Parent and Hazrati, 1995; Lee et al., 2020) and connections between the striatum and substantia nigra (Deniau et al., 1996; Gerfen et al., 1987; Nambu, 2011). The systematic mapping of SNr projection domains into a three-dimensional model (Figure 8A) shows this subnuclear organization additionally extends to basal ganglia output projections to distinct brainstem areas. Thus, rather than operating as a generic hub, the SNr is anatomically posed to subserve functions of discrete basal ganglia module channels, as described for its oculomotor functions (Hikosaka et al., 2014).

Diverse projection neuron populations in SNr collateralize broadly to thalamic nuclei (Figure 6). The lack of electrophysiological specialization of neurons projecting to thalamic nuclei (Figure 5) thus reflects the organization of SNr-thalamus projections is on a particularly fine spatial scale (~100 μm) (Figures 7 and S8). This subnuclear organization of SNr axons appears to correspond with fine-scale subdivisions of projection neurons within thalamus (Aldes, 1988; Berendse and Groenewegen, 1990; Cicirata et al., 1986; Mandelbaum et al., 2019; Smith et al., 2004), which together could underpin subcircuit-specific feedback to cortex and the striatum. The thalamic nuclei targeted by SNr additionally receive topographically organized inputs from the vast majority of newly and previously identified SNr brainstem targets (Krout et al., 2002). Future investigations will be needed to determine whether SNr might have the additional capacity to influence thalamus via disynaptic brainstem-thalamus pathways.

Specificity of Firing Properties in the SNr

SNr projection neurons do not form a homogenous population in terms of their electrophysiological properties (Figures 3–5), and neurons that project to different targets also have significant differences in their intrinsic electrophysiological properties (Figures 4, 5E, and 5F). Taken together, SNr projection populations form a continuum of fast-firing GABAergic neurons that span a broad range of active and passive properties (Figure 3). However, the fine-tuning of intrinsic electrophysiological properties, including spontaneous and maximum firing characteristics, membrane leakiness, and time constants, differentiates SNr projection populations targeting distinct brainstem effector regions (Figures 5E and S6B). Neurons projecting to classic motor structures, i.e., the lateral and central superior colliculus and the pontine and medullary reticular formation, exhibit notably fast intrinsic properties, whereas neurons projecting to neuromodulatory dorsal raphe comprise the slowest population in SNr (Figure 4). Across SNr, projection neurons (Figure 8A) and electrophysiological properties are spatially organized along a medial-lateral gradient, such that the lateral portion of the nucleus is capable of operating at higher rates with faster kinetics (Figure S6C). A corresponding medial-lateral gradient in the distribution of terminals from associative and sensorimotor striatum (Deniau et al., 1996) suggests the medial-lateral axis of electrophysiological specializations in SNr is situated to differentially process outputs of distinct associative versus sensorimotor striatal domains.

All neurons in the SNr have highly linear gain, i.e., firing rate versus input current (Figure 3C), consistent with engineering expectations for motor control circuitry in the excitatory domain (Åström and Murray, 2008). In contrast, the restricted expression of non-linear rebound mechanisms (Figure 4E) alters the signaling capacity of different SNr populations in response to inhibitory inputs, including from the striatum and globus pallidus. In particular, neurons projecting to the medullary reticular formation and inferior colliculus exhibit notable rebound firing (Figure 4E). In neurons that fire tonically, post-inhibitory rebound mechanisms could transform synaptic inhibition into post-synaptic burst firing and/or well-timed spiking, which is likely to differentiate the capacity of direct versus indirect pathway synaptic inputs in rebounding neurons. In contrast, non-rebounding neurons could more linearly integrate inhibitory and excitatory synaptic drives. During behavior, the only well-studied SNr projection, that to the oculomotor superior colliculus, generally disinhibits effector neurons via firing rate decreases (Hikosaka, 2007b), however notable increases in SNr firing rates, driven by unknown circuit mechanism, are commonly observed during diverse behaviors (Gulley et al., 1999; Jin and Costa, 2010). Diversity in SNr intrinsic properties questions whether common disinhibition mechanisms apply to all SNr outputs, which operate across different firing rate ranges (Figures 4 and S5), or whether signaling mechanisms will vary according to the circuit demands of downstream structures.

Behavioral Implications

Many reflexive motor actions are mediated by circuits in which one-to-one projections mediate behavioral responses (Arber, 2012; Buttner-Ennever, 2006; McElvain et al., 2018).

However, the broad collateralization of SNr projections (Figure 6) indicates that simple one-to-one motifs do not underlie basal ganglia circuit mechanisms. Similarly diffuse outputs characterize motor cortical projections (Economo et al., 2018; Kita and Kita, 2012). The broad but specific collateralization pattern of SNr neurons (Figures 6E and 8B) might ensure coherent gating of related behavioral control circuit modules. For example, the SNr projection neurons that target orofacial regions in the medullary reticular formation collateralize to several small brainstem nuclei implicated orofacial sensorimotor signaling (Su5, P5, L5, parabrachial nuclei) and vertical head orientation (InC) (Fukushima, 1987; Kolta et al., 2010) (Figures 6B-E and 8B).

Among the large brainstem targets of SNr, the PPN and midbrain reticular formation are exceptional in that they receive converging collateral input from all projection pools (Figure 6E) and thus are brainstem hubs. Whether these projections mediate general functions, such as muscle tone or arousal (Pienaar et al., 2017), and/or specific functions, such as locomotion, remains to be determined. The PPN is a classic component of the mesencephalic locomotor region (MLR), which mediates striatal effects on locomotion (Garcia-Rill, 1986; Roseberry et al., 2016; Takakusaki et al., 2003). Our data clarify the connections between the SNr and MLR: SNr broadly targets the PPN component and only weekly innervates the high-speed locomotion component, the cuneiform nucleus (Caggiano et al., 2018; Takakusaki et al., 2003) (Figure 2). However, two major nigral targets, the medial superior and inferior colliculi, project extensively to the CnF (Figures S4 and 6E) (Comoli et al., 2012; Ferreira-Pinto et al., 2018; Mitchell et al., 1988). Thus, SNr has diverse paths to the MLR, i.e., indirect to the cuneiform and direct to the PPN and neighboring midbrain reticular formation. All together, various output paths from SNr might support locomotor control under different behavioral contexts and warrant further study.

Basal ganglia outputs via SNr are distinguished from those emitted by GPi in their extensive brainstem targets (Figure 2). However, SNr and GPi share common features in that parvalbumin-expressing GABAergic GPi neurons also target motor and intralaminar thalamic nuclei, as well as the PPN, through collateral projections (Parent and De Bellefeuille, 1982; van der Kooy and Carter, 1981). GPi neurons additionally project to the lateral habenula and thus broadcast in a manner similar to SNr outputs. The second major class of output neurons in GPi, somatostatin-expressing glutamatergic neurons (Shabel et al., 2012; Vincent and Brown, 1986; Wallace et al., 2017), receive striosome input and have putative limbic functions, similar to nigra dopaminergic neurons (Parent and De Bellefeuille, 1982; Rajakumar et al., 1993). All together, the basal ganglia have a broad capacity to directly influence behavioral circuits at diverse levels. The precise roles of each of these projections, outside of the oculomotor system, and their contribution to specific symptoms of basal ganglia pathology remain to be delineated. Although SNr has been shown to be capable of modulating general behavior functions, such as motor vigor (Turner and Desmurget, 2010), the modularity and intrinsic specializations of its outputs imposes specificity and reveals a circuit architecture that can separately control different behaviors.

STAR METHODS

RESOURCE AVAILABILITY

Lead Contact—Further information and requests for resources and reagents should be directed to and will be fulfilled by Dr. David Kleinfeld (dk@physics.ucsd.edu).

Materials Availability—This study did not generate new unique reagents.

Data and Code Availability—The datasets and all code supporting the current study are available from the corresponding author on request.

EXPERIMENTAL MODEL AND SUBJECT DETAILS

All experiments were carried out on mice in accordance with the standards of the Guide for the Care and Use of Laboratory Animals and have been approved by Institutional Animal Care and Use Committee at University of California, San Diego and in accordance with the Champalimaud Center for the Unknown Ethics committee guidelines and approved by the Portuguese Veterinary General Board (Direccao Geral de Veterinaria, Ref. No. 0421/000/000/2014). For electrophysiological studies, 72 C57BL/6J mice aged 4–6 weeks were used; for in situ labeling, 4 C57BL/6J mice aged 8 weeks were used; and for anatomical mappings, 28 6–8-week-old Parvalbumin-Cre (The Jackson Laboratory, Stock # 01730) (Hippenmeyer et al., 2005), VGAT-Cre (The Jackson Laboratory, Stock #028862), or C57BL/6J mice were used. Animals of both sexes were used in each group of experiments.

METHOD DETAILS

Surgical procedures—All surgeries were performed under sterile conditions. For viral tracing experiments, mice were deeply anesthetized with isoflurane and then placed on either a Kopf stereotax or a custom stereotaxic apparatus with a micromanipulator (Sutter MP-285). Mouse body temperature was maintained at 34°C using an animal temperature controller (ATC1000, World Precision Instruments), and isofluorane was maintained at 1.0–1.5 % (v/v) in oxygen at 1.0 – 1.5 l/min throughout the surgery. For anterograde tracing experiments, craniotomies were made in Parvalbumin-Cre (n = 5) or VGAT-Cre (n = 2) mice using a dental drill over the SNr, and each was unilaterally injected with 40 nl of AAV-DJ hSyn-FLEX-mGFP-2A-Synaptophysin-mRuby (titer = 3×10^{13}, Stanford virus core) with a Nanojet II Injector (Drummond Scientific, USA), which infected approximately 40 – 50 % of SNr neurons per experiment. Injections comprised pulses of 4.6 nl/pulse/minute, and pipets were left in place for 15–20 minutes post-injection. Larger injections were avoided due to spillover into neighboring structures. Animals were sacrificed 5 weeks later. For intersectional SNr collateral mapping experiments, each animal was injected with Rabies-G pseudotyped lentivirus expressing Cre (R(G)-lentivirus-hSyn-Cre, Wang lab, MIT) into a single downstream region and AAV2/2-EF1α-DIO-EYFP-WPRE (UNC virus core) into SNr during the same surgery; animals were sacrificed after 6 weeks (n = 18 mice). For genetic- and projection-specific mapping of collaterals, the same protocol was followed for the injection of R(G)-EIAV-DIO-FLP (Lim lab, UCSD) and AAV-DJ-EF1α-fDIO-EYFP (UNC virus core) (n = 3 mice).

For retrograde tracing for electrophysiolgical recordings, SNr target regions in the thalamus and brainstem were targeted for microinjection of Alexa Fluor-594 dextran (10,000 kD; ThermoFisher) in mice aged 4 – 6 week old mice (average: postnatal day 33 ± 5, n = 56 mice). Injections comprised either a supersaturated solution of dextran in sterile water injected using a Nanojet II Injector (Drummond Scientific, USA) or the placement of solid dextran crystals using a custom-made microinjector (0.2 mm outer diameter, 0.1 mm inner diameter; Creative Instruments Development Company) (Marin et al., 2001). The injection pipette/microinjector was left in place for 15 min post-injection. Mice were sacrificed for electrophysiological experiments 3 – 4 days post-injection. All structures were targeted stereotaxically relative to bregma (See also Figure S5).

Histology and staining—For viral tracing experiments, 5–6 weeks post-injection, animals were deeply anesthetized and transcardially perfused with phosphate-buffered saline (PBS) followed by 4 % (w/v) paraformaldehyde (PFA) in PBS. Brains were dissected and post-fixed for 30–60 min in PFA at room temperature, stored overnight at 4°C in PFA, and then transferred to 30 % (w/v) sucrose in PBS 12 – 16 hours later. Serial 30-μm coronal sections were cut on a freezing microtome (Microm). Sections were washed with PBS, stained with Neurotrace 435/455 Blue Fluorescent Nissl Stain (1:200, ThermoFisher), wet mounted, and cover slipped with Fluoromount-G (SouthernBiotech). For dark product labeling (Figure S7), sections were counterstained with cytochrome c (Sigma) and subsequently stained with anti-GFP primary antibody (Novus) and Vectastain Elite ABC kit (Vector laboratories).

For fluorescence in-situ hydridizations, mice were deeply anesthetized with Nembutal and decapitated; brains were rapidly dissected, frozen on dry ice in NEG50, and stored at −80C. Serial 20-μm coronal sections were cut on a cryostat, adhered to SuperFrost Plus Slides, and immediately stored at −80C. Sections were fixed in 4 % PFA in PBS and stained according to Advanced Cell Diagonstics (ACD) RNAscope Multiplex Fluorescent V2 Assay manual, with the exception of a 1:10 dilution of the Protease IV reagent. Probes for Slc32a1, GAD2, Pvalb, and Th mRNA (ACD) were visualized using Opal dyes (Akoya Biosciences). Slides were counterstained with DAPI. Staining was quantified in SNr and, for control, the dentate gyrus of the same sections using cell segmentation according to size and fluorescent intensity in QuPath (Bankhead et al., 2017).

Imaging and anatomical analyses—Whole-brain slide scanning (20X, NA 0.8) was performed on a Zeiss Axio Scan Z.1 and imaged with a 16-bit Hamamatsu Orca 4.0. Images acquired in Zen software (Zeiss) were exported as 16-bit grey scale tiff files (0.325 μm/pixel). To quantify SNr bouton and axon innervation in downstream brain regions, red and green channel tiffs were read into MATLAB and high-pass filtered and thresholded to subtract autofluorescence. Structure boundary ROIs were defined according to criteria in a standard atlas (Franklin and Paxinos, 2013) using the Neurotrace blue channel in ImageJ. Every 3 – 5 sections were quantified for structures > 300 μm and each section quantified for structures < 300 μm. For axonal collateral quantification, axon density was measured in each structure using a standard 400 μm pixel patch, which restricted the quantification to subnuclear domains in thalamus to respect the topographical organization of collaterals in these nuclei.

Three-dimensional reconstructions of the locations of retrogradely labeled SNr neurons were done in Neurolucida (MBF Bioscience). Fluorescently labeled neurons in SNr were marked manually, and contours of SNr, the whole-brain, and nearby landmarks (red nucleus, oculomotor nucleus, and fasciculus retroflexus) were drawn based on Neurotrace Nissl textures. Three-dimensional stacks were generated based on contour boundaries for each experiment, and individual stacks were aligned in Python to a brainstem model (Chen et al., 2019) by rigid global transformations that maximized the overlap of SNr, the red nucleus, and the oculomotor nucleus. The composite reconstruction of SNr topography was rendered using the Visualization Toolkit (VTK) v.7.1.1 in Python.

The topography of SNr collateral projections in thalamus was analyzed using semi-automated pipeline that interfaced MATLAB and Neurolucida. Zeiss CZI files were analyzed in MATLAB using the Bio-formats/MATLAB package, and putative axon terminal zones were automatically identified using segmentation based on intensity and size criteria. Section outlines were automatically contoured based on intensity of the Neurotrace Nissl, and serial sections were automatically stacked based on an iterative closest point (ICP) algorithm of section outlines. Automated MATLAB reconstructions were converted to a Neurolucida-readable format, and Neurolucida was subsequently used to verify the accuracy of automated contouring and axon identifications. Nucleus boundaries were manually contoured based on Neurotrace Nissl textures. Replicate experiments were aligned to corresponding atlas section (Franklin and Paxinos, 2013) using ICP. Topography was quantified based on 1) the Euclidean distances between centroid locations of each axon terminal field and 2) the weighted Jaccard, denoted $J_{W,}$ based on a 50-µm smoothed axon terminal density within thalamic nuclei, such that for each pair of collateral experiments, A and B:

$$Jw(A,B) = \frac{\sum_k \min(A_k, B_k)}{\sum_k \max(A_k, B_k)}$$

where k is the number of samples.

Volumes of neuroanatomical regions downstream of SNr were computed using the combination of a publicly available database and manual corrections as needed. Volumes were computed from the Allen Brain Atlas common coordinate framework (CCF v3) for structures whose CCF boundaries adhered to those commonly used (Franklin and Paxinos, 2013). For structures that were not in the CCF or differed significantly, boundaries were manually drawn onto the Allen Brain Atlas images using the Paxinos criteria to calculate their volume in the CCF space. These structures included: ventroanterior thalamus; parvocellular division of the red nucleus; pararubral region; Pre-Edinger Westphal; the lateral, central, and medial divisions of the superior colliculus; dorso- and ventrolateral periaqueductal gray; precuneiform and cuneiform; rostral interstitial; and prerubral field. Note that no SNr projections were observed in the rostral half of the mediodorsal thalamic nucleus, and measurements of its bouton density and volume were restricted to its caudal half.

Anatomical experiments were excluded from analysis in the following cases: AAV expression spilled into overlaying structures or too few cells were labeled for robust axonal measurements.

Electrophysiological recordings—Mice were deeply anesthetized with Nembutal and decapitated. After rapid dissection in ice cold Ringer's solution (125 mM NaCl, 3.5 mM KCl, 1.0 mM $MgSO_4$, 26 mM $NaHCO_3$, 2.5 mM $CaCl_2$, 1.0 mM NaH_2PO_4, and 11 mM dextrose), 250–300 µm thick coronal slices were cut on a Leica VT1200S vibratome and allowed to recover at 34°C for 30 min. Slices rested at room temperature before being transferred to a recording chamber and being perfused with carbogenated Ringer's containing 125 mM NaCl, 3.5 mM KCl, 1 mM $MgSO_4$, 26 mM $NaHCO_3$, 1.5 mM $CaCl_2$, 1.0 mM NaH_2PO_4, 11 mM dextrose, 100 µM picrotoxin and 2.0 mM kynurenic acid at 34°C.

Patch pipettes were pulled from flame-polished glass (Warner) with resistances of 2–4 MΩ using a pipette puller (Sutter or DMZ). Pipette internal solution contained 140 mM K gluconate, 20 mM HEPES, 8 mM NaCl, 0.1 mM EGTA, 2 mM Mg-ATP, and 0.3 mM Na_2-GTP. Retrogradely labeled neurons were visualized with an epifluorescence 594 filter cube, as well as under infrared differential interference contrast (DIC) illumination with Nomarski optics. Locations of recorded neurons were imaged at 2X under brightfield with condenser aperture reduction for enhanced contrast. Neurons were verified to be in SNr using proximal anatomical landmarks, including the shape and location of the cerebral peduncle, oculomotor nerve, zona incerta, geniculate nuclei, medial and lateral lemnisci, and pontine nuclei. Data were acquired with a Multiclamp 700B, low-pass filtered at 10 kHz and digitized at 40 kHz (ITC-18, HEKA). House-written code in Igor Pro 6 was used for acquisition and analysis. Recordings were corrected for a 14 mV junction potential. Spontaneous firing was measured immediately after break in; maximum firing, gain, rebound measurements made on top of a 10-Hz baseline firing rate. Maximum firing rate was defined as the maximum mean firing rate sustained during a 1-sec-long depolarizing step. Recordings were excluded from analyses if spike height was < 50 mV or series resistance exceeded 15 MΩ.

QUANTIFICATION AND STATISTICAL ANALYSIS

Statistical significance was evaluated for the electrophysiological properties of identified projection populations (Figure 5E) versus those of randomly targeted SNr neurons using the Kruskal-Wallis nonparametric multiple group comparison followed by the Dunn *post hoc* test performed in GraphPad Prism (version 7.0). To evaluate differences in the composite electrophysiological properties of each pair of projection populations (Figure 5F), the property values were z-scored, and the Euclidean distance between each pair of neurons in normalized parameter space was calculated for all neuron pairs across the two populations. Statistical significance was assessed by data resampling: specifically, the calculated mean pairwise Euclidean distance was compared to a null distribution generated by randomly shuffling the identities of the neurons in the two populations in MATLAB.

To quantify differences in the topography of axon collateral fields in thalamic nuclei (Figure 7E), the mean Euclidean distance between the centroids of the collateral field puncta distributions was computed. Statistical significance was assessed by data resampling in MATLAB. Specifically, we first computed the Euclidean distance across experiments from two different target populations and for experimental replicates of the same target populations. We next randomly resampled each puncta distribution with replacement to generate a bootstrapped distribution of distances and identified pairs of target populations for which the centroid distance across the pair was significantly greater. The weighted Jaccard index was used to quantify the overlap extent of collateral fields in thalamus (Figures S8). To assess its significance, first the index was calculated pairwise across replicates and compared to the null distribution of pairwise Jaccard index generated by shuffling the identity of all experiments.

Data are represented as mean ± SEM unless otherwise indicated. The n numbers and p values are reported explicitly in the main text, figures, and figure legends.

Supplementary Material

Refer to Web version on PubMed Central for supplementary material.

Acknowledgements

This work was supported by the European Research Council (R.M.C.), a Howard Hughes Medical Institute grant (R.M.C.), National Institute of Neurological Disorders and Stroke grants T32 NS007220 (L.E.M.), U01 NS107466 (D.K.), U19 NS090595 (D.K.), R01 NS111162 (B.L.B.), U19 NS104649 (R.M.C.), a Tourette Association of America grant (L.E.M.), and equipment funds from the Dr. George Feher Experimental Biophysics Chair. We thank Agnieszka Brzozowska-Prechtl and Beth Friedman for assistance with the histology, Fan Wang (MIT) for providing the retrograde lentivirus, Hannah Leichty and Alexander Newberry for technical support, Jack Glaser of MicroBrightField Bioscience for use of their Neurolucida software and access to “beta” versions of new programs, and Harvey J. Karten for helpful discussions. D.K. attended to the myriad of university rules and forms that govern environmental health and safety, including the ethical use of animals as well as the use of chemicals, controlled substances, cybersecurity, hazardous substances, and viruses.

References

Aldes LD (1988). Thalamic connectivity of rat somatic motor cortex. Brain Res Bull 20, 333–348. [PubMed: 2452673]

Alexander GE, Crutcher MD, and DeLong MR (1990). Basal ganglia-thalamocortical circuits: parallel substrates for motor, oculomotor, “prefrontal” and “limbic” functions. Prog Brain Res 85, 119–146. [PubMed: 2094891]

Alloway KD, Smith JB, and Beauchemin KJ (2010). Quantitative analysis of the bilateral brainstem projections from the whisker and forepaw regions in rat primary motor cortex. J Comp Neurol 518, 4546–4566. [PubMed: 20886621]

Anderson M, and Yoshida M. (1977). Electrophysiological evidence for branching nigral projections to the thalamus and the superior colliculus. Brain Res 137, 361–364. [PubMed: 589460]

Arber S. (2012). Motor circuits in action: specification, connectivity, and function. Neuron 74, 975–989. [PubMed: 22726829]

Arber S, and Costa RM (2018). Connecting neuronal circuits for movement. Science 360, 1403–1404. [PubMed: 29954969]

Asanuma C, Thach WT, and Jones EG (1983). Brainstem and spinal projections of the deep cerebellar nuclei in the monkey, with observations on the brainstem projections of the dorsal column nuclei. Brain Res 286, 299–322. [PubMed: 6189563]

Åström KJ, and Murray RM (2008). Feedback systems : an introduction for scientists and engineers (Princeton: Princeton University Press).

Atherton JF, and Bevan MD (2005). Ionic mechanisms underlying autonomous action potential generation in the somata and dendrites of GABAergic substantia nigra pars reticulata neurons in vitro. J Neurosci 25, 8272–8281. [PubMed: 16148235]

Bankhead P, Loughrey MB, Fernandez JA, Dombrowski Y, McArt DG, Dunne PD, McQuaid S, Gray RT, Murray LJ, Coleman HG, et al. (2017). QuPath: Open source software for digital pathology image analysis. Sci Rep 7, 16878. [PubMed: 29203879]

Beckstead RM, and Frankfurter A. (1982). The distribution and some morphological features of substantia nigra neurons that project to the thalamus, superior colliculus and pedunculopontine nucleus in the monkey. Neuroscience 7, 2377–2388. [PubMed: 7177379]

Bentivoglio M, and Kuypers HG (1982). Divergent axon collaterals from rat cerebellar nuclei to diencephalon, mesencephalon, medulla oblongata and cervical cord. A fluorescent double retrograde labeling study. Exp Brain Res 46, 339–356. [PubMed: 7095042]

Berendse HW, and Groenewegen HJ (1990). Organization of the thalamostriatal projections in the rat, with special emphasis on the ventral striatum. J Comp Neurol 299, 187–228. [PubMed: 2172326]

Brownstone RM, and Chopek JW (2018). Reticulospinal Systems for Tuning Motor Commands. Front Neural Circuits 12, 30. [PubMed: 29720934]

Buttner-Ennever JA (2006). The extraocular motor nuclei: organization and functional neuroanatomy. Prog Brain Res 151, 95–125. [PubMed: 16221587]

Caggiano V, Leiras R, Goni-Erro H, Masini D, Bellardita C, Bouvier J, Caldeira V, Fisone G, and Kiehn O. (2018). Midbrain circuits that set locomotor speed and gait selection. Nature 553, 455–460. [PubMed: 29342142]

Cebrian C, Parent A, and Prensa L. (2005). Patterns of axonal branching of neurons of the substantia nigra pars reticulata and pars lateralis in the rat. J Comp Neurol 492, 349–369. [PubMed: 16217789]

Cebrian C, and Prensa L. (2010). Basal ganglia and thalamic input from neurons located within the ventral tier cell cluster region of the substantia nigra pars compacta in the rat. J Comp Neurol 518, 1283–1300. [PubMed: 20151360]

Chen Y, McElvain LE, Tolpygo AS, Ferrante D, Friedman B, Mitra PP, Karten HJ, Freund Y, and Kleinfeld D. (2019). An active texture-based digital atlas enables automated mapping of structures and markers across brains. Nat Methods 16, 341–350. [PubMed: 30858600]

Chronister RB, Walding JS, Aldes LD, and Marco LA (1988). Interconnections between substantia nigra reticulata and medullary reticular formation. Brain Res Bull 21, 313–317. [PubMed: 3191414]

Cicirata F, Angaut P, Cioni M, Serapide MF, and Papale A. (1986). Functional organization of thalamic projections to the motor cortex. An anatomical and electrophysiological study in the rat. Neuroscience 19, 81–99. [PubMed: 3024065]

Comoli E, Das Neves Favaro P, Vautrelle N, Leriche M, Overton PG, and Redgrave P. (2012). Segregated anatomical input to sub-regions of the rodent superior colliculus associated with approach and defense. Front Neuroanat 6, 9. [PubMed: 22514521]

Dean P, Redgrave P, and Mitchell IJ (1988). Organisation of efferent projections from superior colliculus to brainstem in rat: evidence for functional output channels. Prog Brain Res 75, 27–36. [PubMed: 2847244]

DeLong MR, Crutcher MD, and Georgopoulos AP (1983). Relations between movement and single cell discharge in the substantia nigra of the behaving monkey. J Neurosci 3, 1599–1606. [PubMed: 6875659]

DeLong M.R.a.G.A.P. (2011). Motor Functions of the Basal Ganglia. In Comprehensive Physiology.

Deniau JM, Hammond-Le Guyader C, Feger J, and McKenzie JS (1977). Bilateral projection of nigro-collicular neurons: An electrophysiological analysis in the rat. Neurosci Lett 5, 45–50. [PubMed: 19604969]

Deniau JM, Menetrey A, and Charpier S. (1996). The lamellar organization of the rat substantia nigra pars reticulata: segregated patterns of striatal afferents and relationship to the topography of corticostriatal projections. Neuroscience 73, 761–781. [PubMed: 8809796]

Drager UC, and Hubel DH (1976). Topography of visual and somatosensory projections to mouse superior colliculus. J Neurophysiol 39, 91–101. [PubMed: 1249606]

Economo MN, Viswanathan S, Tasic B, Bas E, Winnubst J, Menon V, Graybuck LT, Nguyen TN, Smith KA, Yao Z, et al. (2018). Distinct descending motor cortex pathways and their roles in movement. Nature 563, 79–84. [PubMed: 30382200]

Ferreira-Pinto MJ, Ruder L, Capelli P, and Arber S. (2018). Connecting Circuits for Supraspinal Control of Locomotion. Neuron 100, 361–374. [PubMed: 30359602]

Franklin KBJ, and Paxinos G. (2013). Paxinos and Franklin’s The mouse brain in stereotaxic coordinates, Fourth edition. edn (Amsterdam: Academic Press, an imprint of Elsevier).

Fukushima K. (1987). The interstitial nucleus of Cajal and its role in the control of movements of head and eyes. Prog Neurobiol 29, 107–192. [PubMed: 3108957]

Gabbott PL, Warner TA, Jays PR, Salway P, and Busby SJ (2005). Prefrontal cortex in the rat: projections to subcortical autonomic, motor, and limbic centers. J Comp Neurol 492, 145–177. [PubMed: 16196030]

Garcia-Rill E. (1986). The basal ganglia and the locomotor regions. Brain Res 396, 47–63. [PubMed: 2871904]

Gerfen CR, Herkenham M, and Thibault J. (1987). The neostriatal mosaic: II. Patch- and matrix-directed mesostriatal dopaminergic and non-dopaminergic systems. J Neurosci 7, 3915–3934. [PubMed: 2891799]

Gervasoni D, Peyron C, Rampon C, Barbagli B, Chouvet G, Urbain N, Fort P, and Luppi PH (2000). Role and origin of the GABAergic innervation of dorsal raphe serotonergic neurons. J Neurosci 20, 4217–4225. [PubMed: 10818157]

Gonzalez-Hernandez T, Barroso-Chinea P, Acevedo A, Salido E, and Rodriguez M. (2001). Colocalization of tyrosine hydroxylase and GAD65 mRNA in mesostriatal neurons. Eur J Neurosci 13, 57–67. [PubMed: 11135004]

Gonzalez-Hernandez T, and Rodriguez M. (2000). Compartmental organization and chemical profile of dopaminergic and GABAergic neurons in the substantia nigra of the rat. J Comp Neurol 421, 107–135. [PubMed: 10813775]

Graybiel AM, and Ragsdale CW Jr. (1979). Fiber connections of the basal ganglia. Prog Brain Res 51, 237–283. [PubMed: 399353]

Grillner S. (2006). Biological pattern generation: the cellular and computational logic of networks in motion. Neuron 52, 751–766. [PubMed: 17145498]

Gulley JM, Kosobud AE, and Rebec GV (2002). Behavior-related modulation of substantia nigra pars reticulata neurons in rats performing a conditioned reinforcement task. Neuroscience 111, 337–349. [PubMed: 11983319]

Gulley JM, Kuwajima M, Mayhill E, and Rebec GV (1999). Behavior-related changes in the activity of substantia nigra pars reticulata neurons in freely moving rats. Brain Res 845, 68–76. [PubMed: 10529445]

Haber SN, and Calzavara R. (2009). The cortico-basal ganglia integrative network: the role of the thalamus. Brain Res Bull 78, 69–74. [PubMed: 18950692]

Hikosaka O. (2007a). Basal ganglia mechanisms of reward-oriented eye movement. Ann N Y Acad Sci 1104, 229–249. [PubMed: 17360800]

Hikosaka O. (2007b). GABAergic output of the basal ganglia. Prog Brain Res 160, 209–226. [PubMed: 17499116]

Hikosaka O, Kim HF, Yasuda M, and Yamamoto S. (2014). Basal ganglia circuits for reward value-guided behavior. Annu Rev Neurosci 37, 289–306. [PubMed: 25032497]

Hikosaka O, and Wurtz RH (1983). Visual and oculomotor functions of monkey substantia nigra pars reticulata. I. Relation of visual and auditory responses to saccades. J Neurophysiol 49, 1230–1253. [PubMed: 6864248]

Hintiryan H, Foster NN, Bowman I, Bay M, Song MY, Gou L, Yamashita S, Bienkowski MS, Zingg B, Zhu M, et al. (2016). The mouse cortico-striatal projectome. Nat Neurosci 19, 1100–1114. [PubMed: 27322419]

Hippenmeyer S, Vrieseling E, Sigrist M, Portmann T, Laengle C, Ladle DR, and Arber S. (2005). A developmental switch in the response of DRG neurons to ETS transcription factor signaling. PLoS Biol 3, e159. [PubMed: 15836427]

Holmes AL, Forcelli PA, DesJardin JT, Decker AL, Teferra M, West EA, Malkova L, and Gale K. (2012). Superior colliculus mediates cervical dystonia evoked by inhibition of the substantia nigra pars reticulata. J Neurosci 32, 13326–13332. [PubMed: 22993447]

Holstege G. (1987). Some anatomical observations on the projections from the hypothalamus to brainstem and spinal cord: an HRP and autoradiographic tracing study in the cat. J Comp Neurol 260, 98–126. [PubMed: 3496365]

Hopkins DA, and Holstege G. (1978). Amygdaloid projections to the mesencephalon, pons and medulla oblongata in the cat. Exp Brain Res 32, 529–547. [PubMed: 689127]

Jaccard P. (1912). The distribution of the flora in the alpine zone. New Phytologist 11, 37–50.

Jeong M, Kim Y, Kim J, Ferrante DD, Mitra PP, Osten P, and Kim D. (2016). Comparative three-dimensional connectome map of motor cortical projections in the mouse brain. Sci Rep 6, 20072. [PubMed: 26830143]

Jin X, and Costa RM (2010). Start/stop signals emerge in nigrostriatal circuits during sequence learning. Nature 466, 457–462. [PubMed: 20651684]

Jin X, and Costa RM (2015). Shaping action sequences in basal ganglia circuits. Curr Opin Neurobiol 33, 188–196. [PubMed: 26189204]

Jurgens U. (2002). Neural pathways underlying vocal control. Neurosci Biobehav Rev 26, 235–258. [PubMed: 11856561]

Kita T, and Kita H. (2012). The subthalamic nucleus is one of multiple innervation sites for long-range corticofugal axons: a single-axon tracing study in the rat. J Neurosci 32, 5990–5999. [PubMed: 22539859]

Klaus A, da Silva JA, and Costa RM (2019). What, If, and When to Move: Basal Ganglia Circuits and Self-Paced Action Initiation. Annu Rev Neurosci.

Kolkman KE, McElvain LE, and du Lac S. (2011). Diverse precerebellar neurons share similar intrinsic excitability. J Neurosci 31, 16665–16674. [PubMed: 22090493]

Kolta A, Morquette P, Lavoie R, Arsenault I, and Verdier D. (2010). Modulation of rhythmogenic properties of trigeminal neurons contributing to the masticatory CPG. Prog Brain Res 187, 137–148. [PubMed: 21111205]

Krout KE, Belzer RE, and Loewy AD (2002). Brainstem projections to midline and intralaminar thalamic nuclei of the rat. J Comp Neurol 448, 53–101. [PubMed: 12012375]

Kuypers HGJM (1981). Anatomy of the Descending Pathways. In Handbook of Physiology; Nervous System II (American Physiological Society), pp. 597–666.

Lee J, Wengang Wang W, and Sabatini BL (2020). Anatomically segregated basal ganglia pathways allow parallel behavioral modulation. Nat Neurosci 23, 1388–1398. [PubMed: 32989293]

Liang H, Paxinos G, and Watson C. (2011). Projections from the brain to the spinal cord in the mouse. Brain Struct Funct 215, 159–186. [PubMed: 20936329]

Mandelbaum G, Taranda J, Haynes TM, Hochbaum DR, Huang KW, Hyun M, Umadevi Venkataraju K, Straub C, Wang W, Robertson K, et al. (2019). Distinct Cortical-Thalamic-Striatal Circuits through the Parafascicular Nucleus. Neuron 102, 636–652 e637. [PubMed: 30905392]

Marin G, Henny P, Letelier JC, Sentis E, Karten H, Mrosko B, and Mpodozis J. (2001). A simple method to microinject solid neural tracers into deep structures of the brain. J Neurosci Methods 106, 121–129. [PubMed: 11325431]

May PJ, Billig I, Gamlin PD, and Quinet J. (2019). Central mesencephalic reticular formation control of the near response: lens accommodation circuits. J Neurophysiol 121, 1692–1703. [PubMed: 30840529]

McElvain LE, Bagnall MW, Sakatos A, and du Lac S. (2010). Bidirectional plasticity gated by hyperpolarization controls the gain of postsynaptic firing responses at central vestibular nerve synapses. Neuron 68, 763–775. [PubMed: 21092864]

McElvain LE, Friedman B, Karten HJ, Svoboda K, Wang F, Deschenes M, and Kleinfeld D. (2018). Circuits in the rodent brainstem that control whisking in concert with other orofacial motor actions. Neuroscience 368, 152–170. [PubMed: 28843993]

Mena-Segovia J, Bolam JP, and Magill PJ (2004). Pedunculopontine nucleus and basal ganglia: distant relatives or part of the same family? Trends Neurosci 27, 585–588. [PubMed: 15374668]

Mink JW (2001). Basal ganglia dysfunction in Tourette's syndrome: a new hypothesis. Pediatr Neurol 25, 190–198. [PubMed: 11587872]

Mitchell IJ, Dean P, and Redgrave P. (1988). The projection from superior colliculus to cuneiform area in the rat. II. Defence-like responses to stimulation with glutamate in cuneiform nucleus and surrounding structures. Exp Brain Res 72, 626–639. [PubMed: 3234506]

Nambu A. (2011). Somatotopic organization of the primate Basal Ganglia. Front Neuroanat 5, 26. [PubMed: 21541304]

Nelson AB, and Kreitzer AC (2014). Reassessing models of basal ganglia function and dysfunction. Annu Rev Neurosci 37, 117–135. [PubMed: 25032493]

Parent A, and De Bellefeuille L. (1982). Organization of efferent projections from the internal segment of globus pallidus in primate as revealed by fluorescence retrograde labeling method. Brain Res 245, 201–213. [PubMed: 7127069]

Parent A, and Hazrati LN (1995). Functional anatomy of the basal ganglia. I. The cortico-basal ganglia-thalamo-cortical loop. Brain Res Brain Res Rev 20, 91–127. [PubMed: 7711769]

Parent A, Mackey A, Smith Y, and Boucher R. (1983). The output organization of the substantia nigra in primate as revealed by a retrograde double labeling method. Brain Res Bull 10, 529–537. [PubMed: 6305462]

Peters AJ, Liu H, and Komiyama T. (2017). Learning in the Rodent Motor Cortex. Annu Rev Neurosci 40, 77–97. [PubMed: 28375768]

Pienaar IS, Vernon A, and Winn P. (2017). The Cellular Diversity of the Pedunculopontine Nucleus: Relevance to Behavior in Health and Aspects of Parkinson's Disease. Neuroscientist 23, 415–431. [PubMed: 27932591]

Pollak Dorocic I, Furth D, Xuan Y, Johansson Y, Pozzi L, Silberberg G, Carlen M, and Meletis K. (2014). A whole-brain atlas of inputs to serotonergic neurons of the dorsal and median raphe nuclei. Neuron 83, 663–678. [PubMed: 25102561]

Prensa L, and Parent A. (2001). The nigrostriatal pathway in the rat: A single-axon study of the relationship between dorsal and ventral tier nigral neurons and the striosome/matrix striatal compartments. J Neurosci 21, 7247–7260. [PubMed: 11549735]

Rajakumar N, Elisevich K, and Flumerfelt BA (1993). Compartmental origin of the striato-entopeduncular projection in the rat. J Comp Neurol 331, 286–296. [PubMed: 8509503]

Raymond JL, and Medina JF (2018). Computational Principles of Supervised Learning in the Cerebellum. Annu Rev Neurosci 41, 233–253. [PubMed: 29986160]

Redgrave P, Mitchell IJ, and Dean P. (1987a). Descending projections from the superior colliculus in rat: a study using orthograde transport of wheatgerm-agglutinin conjugated horseradish peroxidase. Exp Brain Res 68, 147–167. [PubMed: 2826204]

Redgrave P, Mitchell IJ, and Dean P. (1987b). Further evidence for segregated output channels from superior colliculus in rat: ipsilateral tecto-pontine and tecto-cuneiform projections have different cells of origin. Brain Res 413, 170–174. [PubMed: 3594255]

Richards CD, Shiroyama T, and Kitai ST (1997). Electrophysiological and immunocytochemical characterization of GABA and dopamine neurons in the substantia nigra of the rat. Neuroscience 80, 545–557. [PubMed: 9284356]

Risold PY, Thompson RH, and Swanson LW (1997). The structural organization of connections between hypothalamus and cerebral cortex. Brain Res Brain Res Rev 24, 197–254. [PubMed: 9385455]

Robbins JA, Logemann JA, and Kirshner HS (1986). Swallowing and speech production in Parkinson's disease. Ann Neurol 19, 283–287. [PubMed: 3963773]

Roseberry TK, Lee AM, Lalive AL, Wilbrecht L, Bonci A, and Kreitzer AC (2016). Cell-Type-Specific Control of Brainstem Locomotor Circuits by Basal Ganglia. Cell 164, 526–537. [PubMed: 26824660]

Rossi MA, Li HE, Lu D, Kim IH, Bartholomew RA, Gaidis E, Barter JW, Kim N, Cai MT, Soderling SH, et al. (2016). A GABAergic nigrotectal pathway for coordination of drinking behavior. Nat Neurosci 19, 742–748. [PubMed: 27043290]

Schiebel AB (2011). The Brain Stem Reticular Core and Sensory Function. In Comprehensive Physiology.

Schneider JS, Manetto C, and Lidsky TI (1985). Substantia nigra projection to medullary reticular formation: relevance to oculomotor and related motor functions in the cat. Neurosci Lett 62, 1–6. [PubMed: 2999652]

Sesack SR, Deutch AY, Roth RH, and Bunney BS (1989). Topographical organization of the efferent projections of the medial prefrontal cortex in the rat: an anterograde tract-tracing study with Phaseolus vulgaris leucoagglutinin. J Comp Neurol 290, 213–242. [PubMed: 2592611]

Shabel SJ, Proulx CD, Trias A, Murphy RT, and Malinow R. (2012). Input to the lateral habenula from the basal ganglia is excitatory, aversive, and suppressed by serotonin. Neuron 74, 475–481. [PubMed: 22578499]

Smith Y, Raju DV, Pare JF, and Sidibe M. (2004). The thalamostriatal system: a highly specific network of the basal ganglia circuitry. Trends Neurosci 27, 520–527. [PubMed: 15331233]

Stanek E.t., Cheng S, Takatoh J, Han BX, and Wang F. (2014). Monosynaptic premotor circuit tracing reveals neural substrates for oro-motor coordination. Elife 3, e02511. [PubMed: 24843003]

Svoboda K, and Li N. (2018). Neural mechanisms of movement planning: motor cortex and beyond. Curr Opin Neurobiol 49, 33–41. [PubMed: 29172091]

Takakusaki K, Habaguchi T, Ohtinata-Sugimoto J, Saitoh K, and Sakamoto T. (2003). Basal ganglia efferents to the brainstem centers controlling postural muscle tone and locomotion: a new concept for understanding motor disorders in basal ganglia dysfunction. Neuroscience 119, 293–308. [PubMed: 12763089]

Towe AL, and Luschei ES (2013). Motor Coordination (Springer US).

Turner RS, and Desmurget M. (2010). Basal ganglia contributions to motor control: a vigorous tutor. Curr Opin Neurobiol 20, 704–716. [PubMed: 20850966]

Utter AA, and Basso MA (2008). The basal ganglia: an overview of circuits and function. Neurosci Biobehav Rev 32, 333–342. [PubMed: 17202023]

van der Kooy D, and Carter DA (1981). The organization of the efferent projections and striatal afferents of the entopeduncular nucleus and adjacent areas in the rat. Brain Res 211, 15–36. [PubMed: 6164450]

Vincent SR, and Brown JC (1986). Somatostatin immunoreactivity in the entopeduncular projection to the lateral habenula in the rat. Neurosci Lett 68, 160–164. [PubMed: 2875419]

Visser JE, and Bloem BR (2005). Role of the basal ganglia in balance control. Neural Plast 12, 161–174; discussion 263–172. [PubMed: 16097484]

Von Krosigk M, and Smith AD (1991). Descending Projections from the Substantia Nigra and Retrorubral Field to the Medullary and Pontomedullary Reticular Formation. Eur J Neurosci 3, 260–273. [PubMed: 12106204]

Wallace ML, Saunders A, Huang KW, Philson AC, Goldman M, Macosko EZ, McCarroll SA, and Sabatini BL (2017). Genetically Distinct Parallel Pathways in the Entopeduncular Nucleus for Limbic and Sensorimotor Output of the Basal Ganglia. Neuron 94, 138–152 e135. [PubMed: 28384468]

Wang S, and Redgrave P. (1997). Microinjections of muscimol into lateral superior colliculus disrupt orienting and oral movements in the formalin model of pain. Neuroscience 81, 967–988. [PubMed: 9330360]

Yasui Y, Nakano K, Nakagawa Y, Kayahara T, Shiroyama T, and Mizuno N. (1992). Non-dopaminergic neurons in the substantia nigra project to the reticular formation around the trigeminal motor nucleus in the rat. Brain Res 585, 361–366. [PubMed: 1380874]

Yasui Y, Tsumori T, Ando A, Domoto T, Kayahara T, and Nakano K. (1994). Descending projections from the superior colliculus to the reticular formation around the motor trigeminal nucleus and the parvicellular reticular formation of the medulla oblongata in the rat. Brain Res 656, 420–426. [PubMed: 7529641]

Highlights

- SNr neurons project to diverse structures throughout the diencephalon and brainstem
- Neuronal subsets project differentially and strongly to distinct brainstem targets
- Neuronal subsets differ in their subthreshold and spiking electrophysiology
- Neuronal subsets also form collaterals that universally include PPN and thalamus

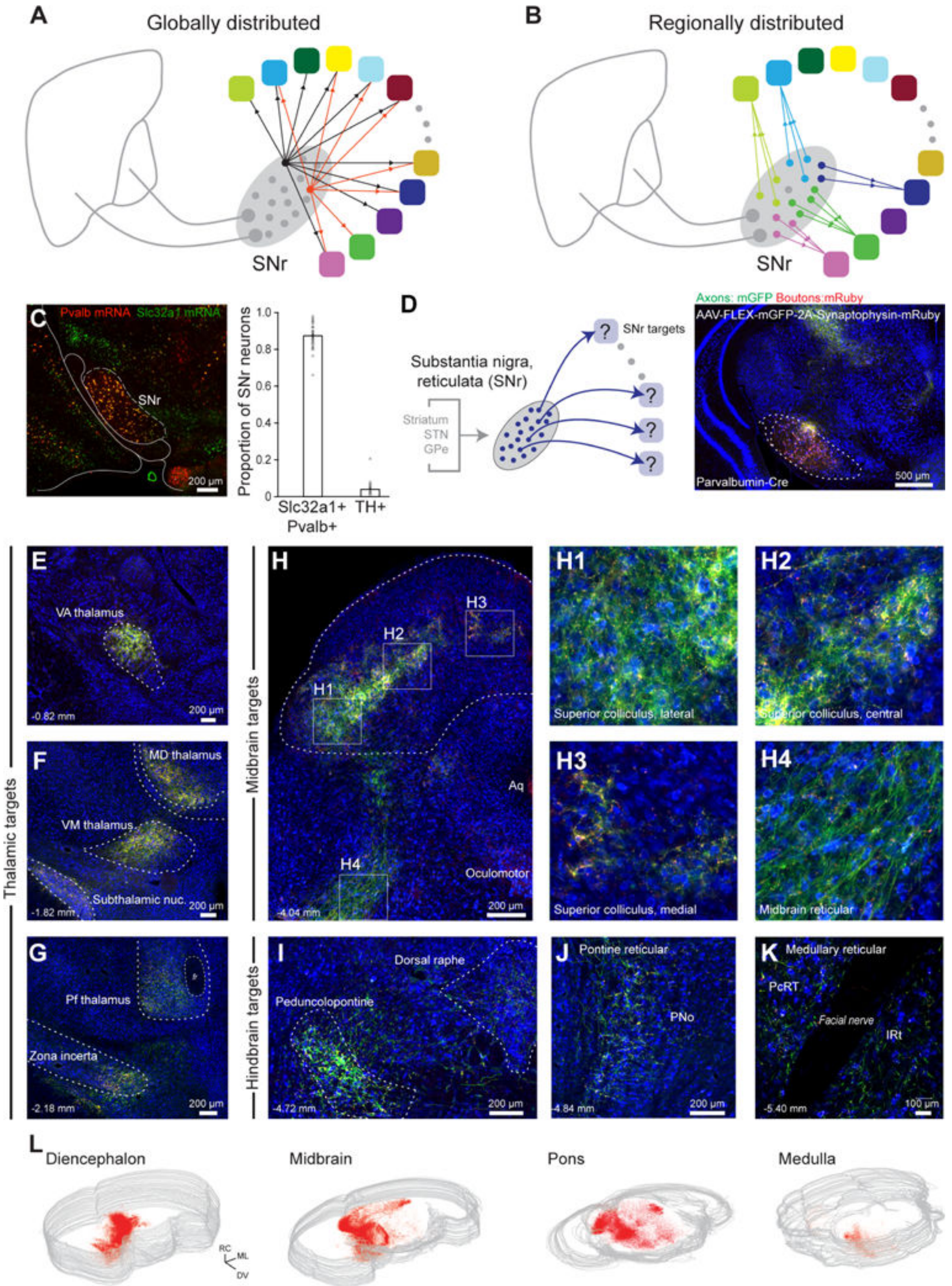

Figure 1. Brain-wide axonal projection pattern from SNr.

(A) Schematic of potential global architecture where intermixed SNr neurons project to all target regions with equal probability, although not necessarily equal axonal density.

(B) Schematic of potential regionally divided architecture where different pools of neurons project to each target and, further, the projection pools are spatially segregated.

(C) Representative in situ hybridization of Pvalb (red) and Slc32a1 (green) mRNA in SNr (left). Proportion of Pvalb+ GABAergic and Th+ dopaminergic neurons in SNr (right, 39 sections). Error bars = SEM.

(D) Anterograde tracing of SNr projections labeled with AAV-DJ-hSyn-FLEX-mGFP-2A-Synaptophysin-mRuby injected into SNr of a PV-Cre mouse.

(E-K) Whole-brain, high-resolution (0.325 μm/pixel) slide scanning of SNr axons (green) and boutons (red) demonstrates projections to (panels E-G) motor and intralaminar/midline thalamus, subthalamic, and incertal nuclei, (panels H1-H3) domains of the superior colliculus, and (panels H4, I-K) diverse premotor brainstem regions, including midbrain, pontine, and medullary reticular formations.

(L) Spatial distribution of Synaptophysin-mRuby labeled SNr boutons in 3D reconstructions of the diencephalon and general divisions of the brainstem. See also Figure S1.

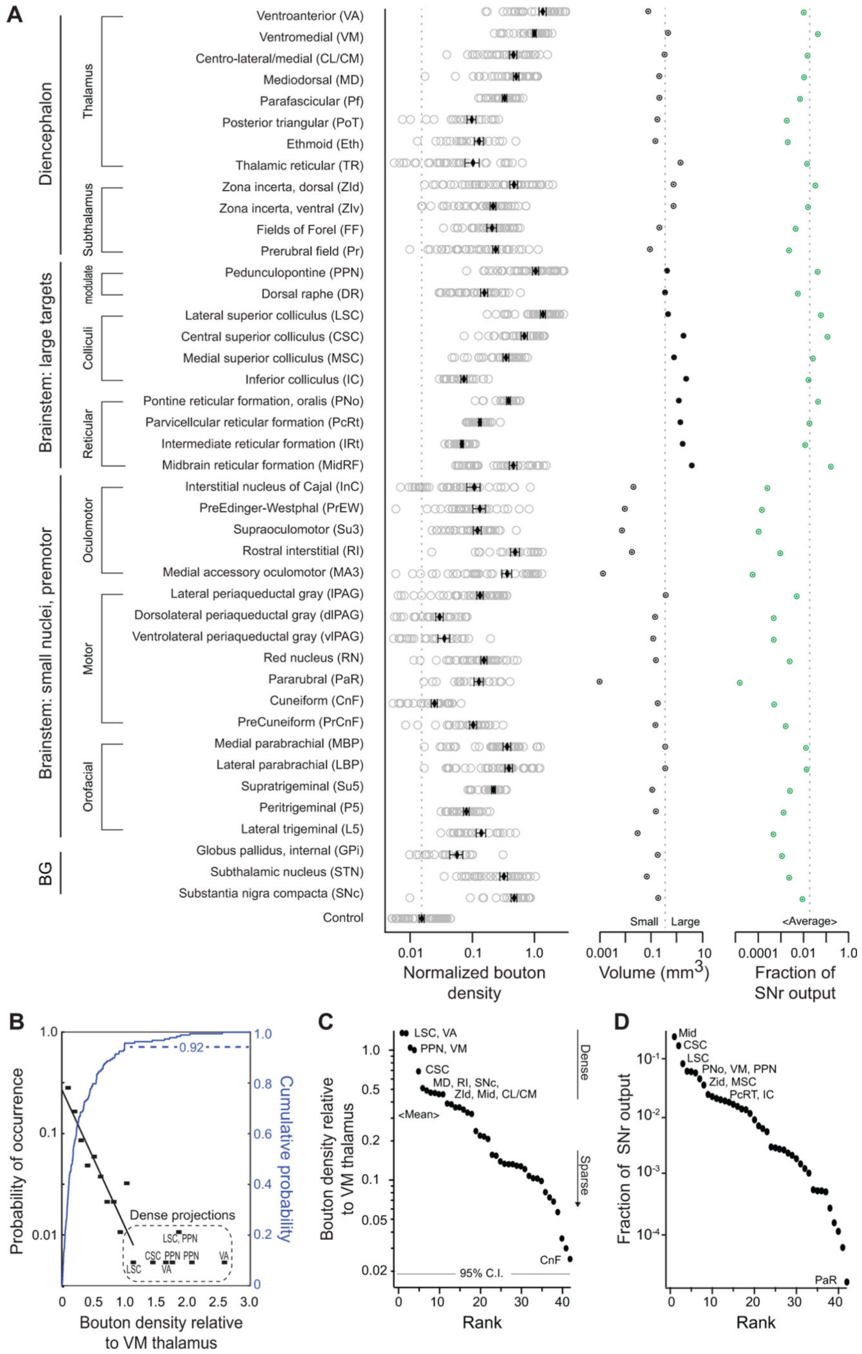

Figure 2. Density and distribution of SNr terminal fields in diverse thalamus and brainstem regions.

(A) (Left) Average bouton density in each of 42 identified target structures, normalized to the density in VM motor thalamus (5 mice). (Middle) Target structure volumes and (right) proportion of total SNr bouton output. Error bars = SEM.

(B) Probability density function (black) and cumulative probability (blue) of bouton density across all targets, relative to VM thalamus.

(C) Rank ordered bouton densities. Most densely innervated targets are motor thalamus (VA/VM), pedunculopontine nucleus (PPN), and central (CSC) and lateral domains (LSC) of the superior colliculus and weakest is the Cuneiform nucleus (CnF). Gray line is 95 % confidence interval of background autofluorescence.

(D) Rank order of proportion of SNr bouton output per structure, calculated from mean bouton density and structure volume. See also Figures S2 and S3.

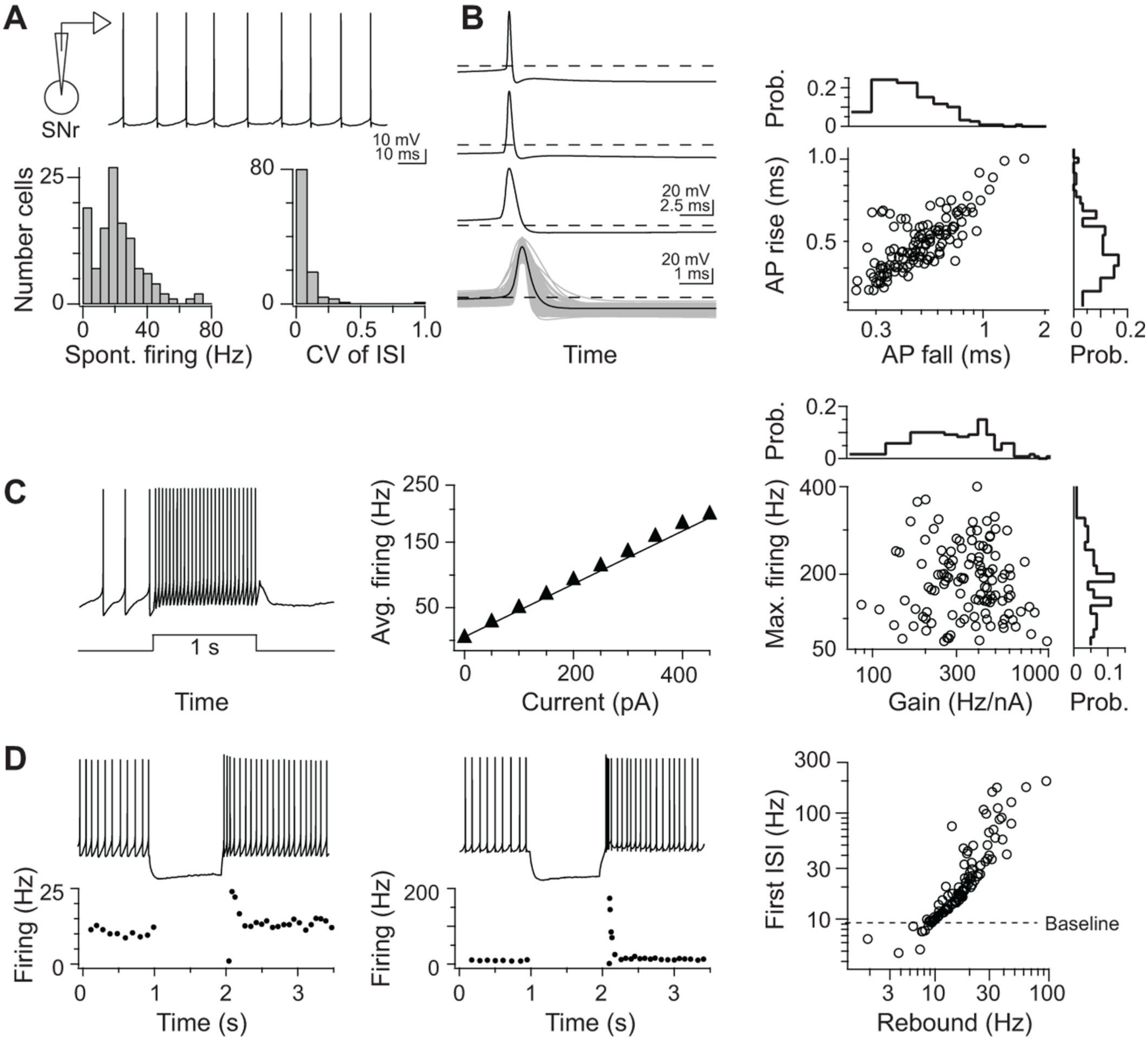

Figure 3. Continuum of intrinsic electrophysiological properties in SNr.

Whole-cell patch-clamp recordings of SNr neurons *in vitro* (120 cells).

(A) Top: Representative current-clamp trace of spontaneous SNr firing. Bottom: histograms of spontaneously firing rates (mean = 21 ± 15 Hz) and inter-spike interval (CV = 0.1 ± 0.1) in SNr.

(B) Left: three example action potential waveforms and the mean waveform (bottom) overlaid with all recorded waveforms (grey). Right: action potential waveforms in SNr neurons are characterized by highly correlated rise and fall durations.

(C) Left: 1-s depolarizing current step injected into an SNr neuron evokes a sustained higher firing. Middle: evoked firing rates increase as a linear function of current over a wide range. Right: across the SNr populations, the capacity to sustain fast-firing and the sensitivity to current inputs (neuronal gain) varied over a >10 fold range, but the mean firing responses increased linearly to depolarization in all neurons ($R^2 = 0.99 \pm 0.01$).

(D) Non-linear firing responses to hyperpolarizing inputs in two neurons, which display (left) modest and (middle) robust post-inhibitory rebound firing from a 10-Hz baseline rate. The SNr population displays heterogeneous responses to hyperpolarization, quantified as the first post-inhibitory instantaneous rate and the rate sustained over 200 ms.

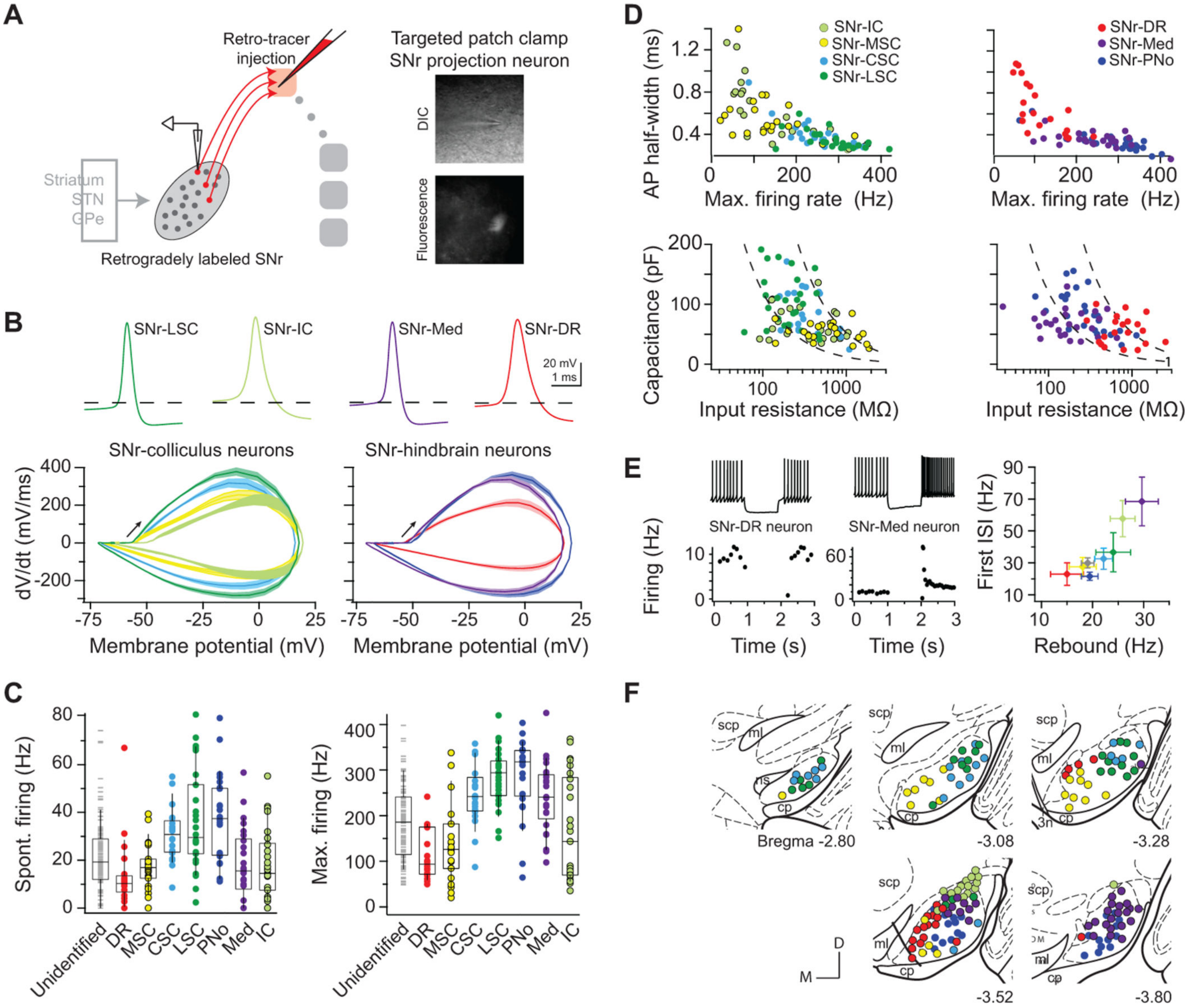

Figure 4. Specialized SNr subpopulations innervate large, functionally distinct brainstem regions.

(A) SNr projection neurons were labeled via retrograde tracer injection into a single downstream brainstem region in each animal, and whole-cell recordings were targeted to fluorescent, retrogradely labeled SNr neurons. 4–7 mice per each target.

(B) Average action potential waveforms and phase-plot kinetics of identified projection neurons. Left: SNr-LSC (green), SNr-CSC (light blue), SNr-MSC (yellow), and SNr-IC (light green) neurons. Right: SNr-PNo (dark blue), SNr-Med (purple), and SNr-DR (red) neurons.

(C) Range of spontaneous and maximum firing rates across projection neuron pools and in randomly targeted SNr neurons (grey). Box plots show quartiles and median (boxes) and 10 – 90% range (whiskers).

(D) Active (top) and passive (bottom) properties of projection neurons fall on a continuum.

(E) SNr neurons projecting to brainstem areas span a range of post-inhibitory rebound firing capabilities. (Left) Example neuron projecting to the dorsal raphe (DR) exhibited no increase in firing in response to hyperpolarization, whereas example neuron projecting to the medullary reticular (Med) exhibited robust rebound firing capabilities. (Right) Average transient and sustained rebound firing rates of each brainstem projection population. Error bars = SEM.

(F) Topographical distributions of SNr projection neuron recording locations, registered to five atlas coronal sections. See also Figures S4-S6.

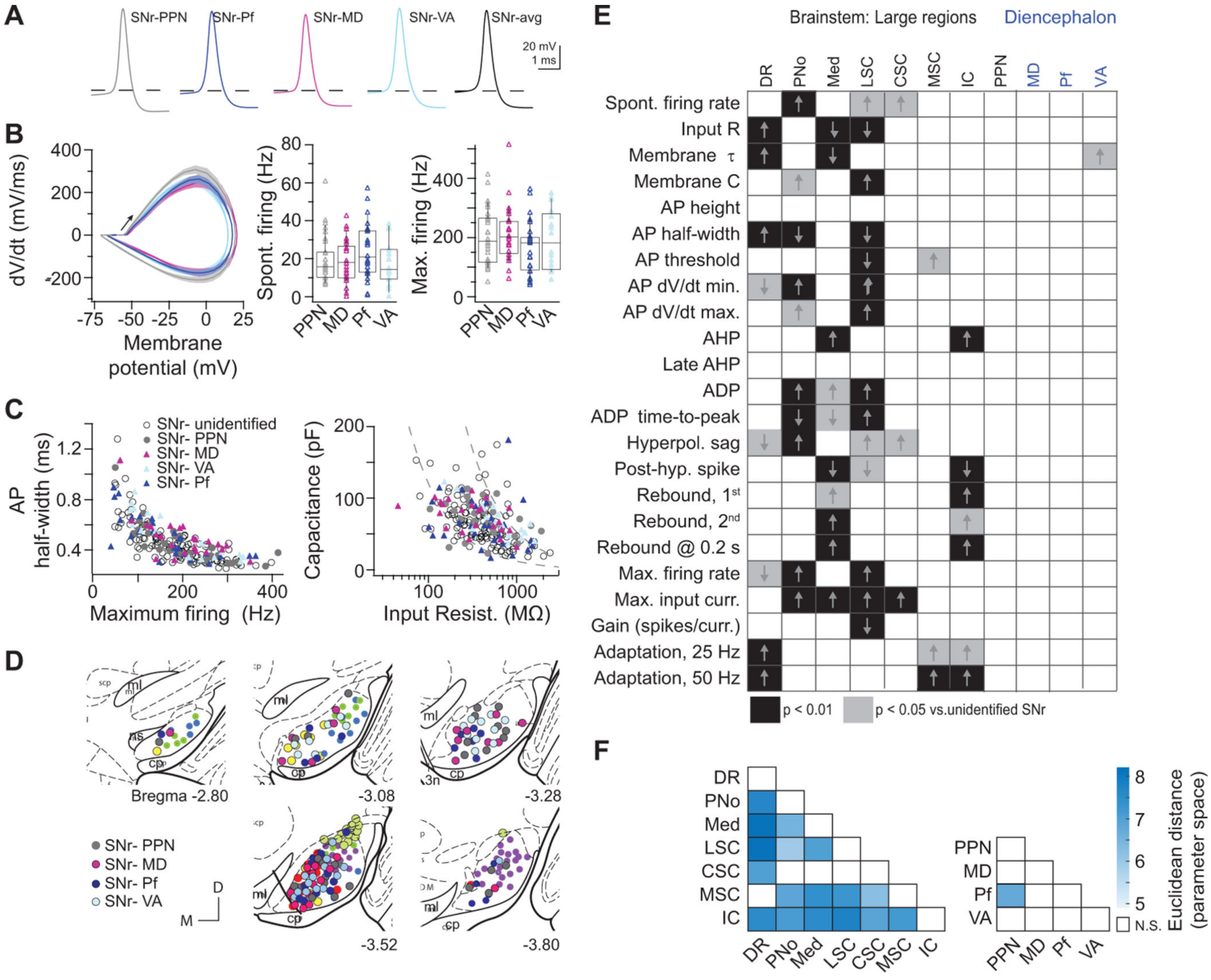

	DR	PNo	Med	LSC	CSC	MSC	IC	PPN	MD	Pf	VA
Spont. firing rate		■↑		▨↑	▨↑						
Input R	■↑		■↓	■↓							
Membrane τ	■↑		■↓								▨↑
Membrane C		▨↑		■↑							
AP height											
AP half-width	■↑	■↓		■↓							
AP threshold				■↓		▨↑					
AP dV/dt min.	▨↓	■↑		■↑							
AP dV/dt max.		▨↑		■↑							
AHP			■↑				■↑				
Late AHP											
ADP		■↑	▨↑	■↑							
ADP time-to-peak		■↓	▨↓	■↑							
Hyperpol. sag	▨↓	■↑		▨↑	▨↑						
Post-hyp. spike			■↓	▨↓			■↓				
Rebound, 1st			▨↑				■↑				
Rebound, 2nd			■↑				▨↑				
Rebound @ 0.2 s			■↑				■↑				
Max. firing rate	▨↓	■↑		■↑							
Max. input curr.		■↑	■↑	■↑	■↑						
Gain (spikes/curr.)				■↓							
Adaptation, 25 Hz	■↑					▨↑	▨↑				
Adaptation, 50 Hz	■↑					■↑	■↑				

■ p < 0.01 ▨ p < 0.05 vs.unidentified SNr

Figure 5. SNr neurons projecting to pedunculopontine and thalamic nuclei are broadly distributed in SNr and electrophysiologically heterogeneous.

(A) Average action potential waveforms of SNr neurons labeled via retrograde tracer injection into the pedunculopontine (PPN, grey), mediodorsal nuclei (MD, magenta), parafascicular (Pf, dark blue) or ventroanterior (VA, light blue) 3–5 mice per each target.

(B) Action potential kinetics (left) and range of spontaneous and maximum firing rates of labeled projection neurons (right). Box plots show quartiles and median (boxes) and 10–90% range (whiskers).

(C) Distributions of projection neuronal populations overlaid with the full diversity of SNr electrophysiological properties (open circles).

(D) Broad topographical distributions of SNr projection neuron recording locations, registered to five atlas coronal sections.

(E) Chart of statistical significance of (rows) intrinsic properties in (columns) retrogradely labeled populations compared to unlabeled SNr neurons (403 neurons across 72 mice). Kruskal-Wallis and Dunn post-hoc tests for significant differences at the $p < 0.05$ (grey) and

$p < 0.01$ (black) levels. Arrows indicate whether value was larger or smaller in retrogradely labeled population.

(F) Quantification of pairwise differences between composite electrophysiological properties in retrogradely labeled SNr populations. Heat map of Euclidean distances computed from z-scored electrophysiological properties; intensity corresponds to the distance. White = not statistically different, $p < 0.01$. See also Figures S5 and S6.

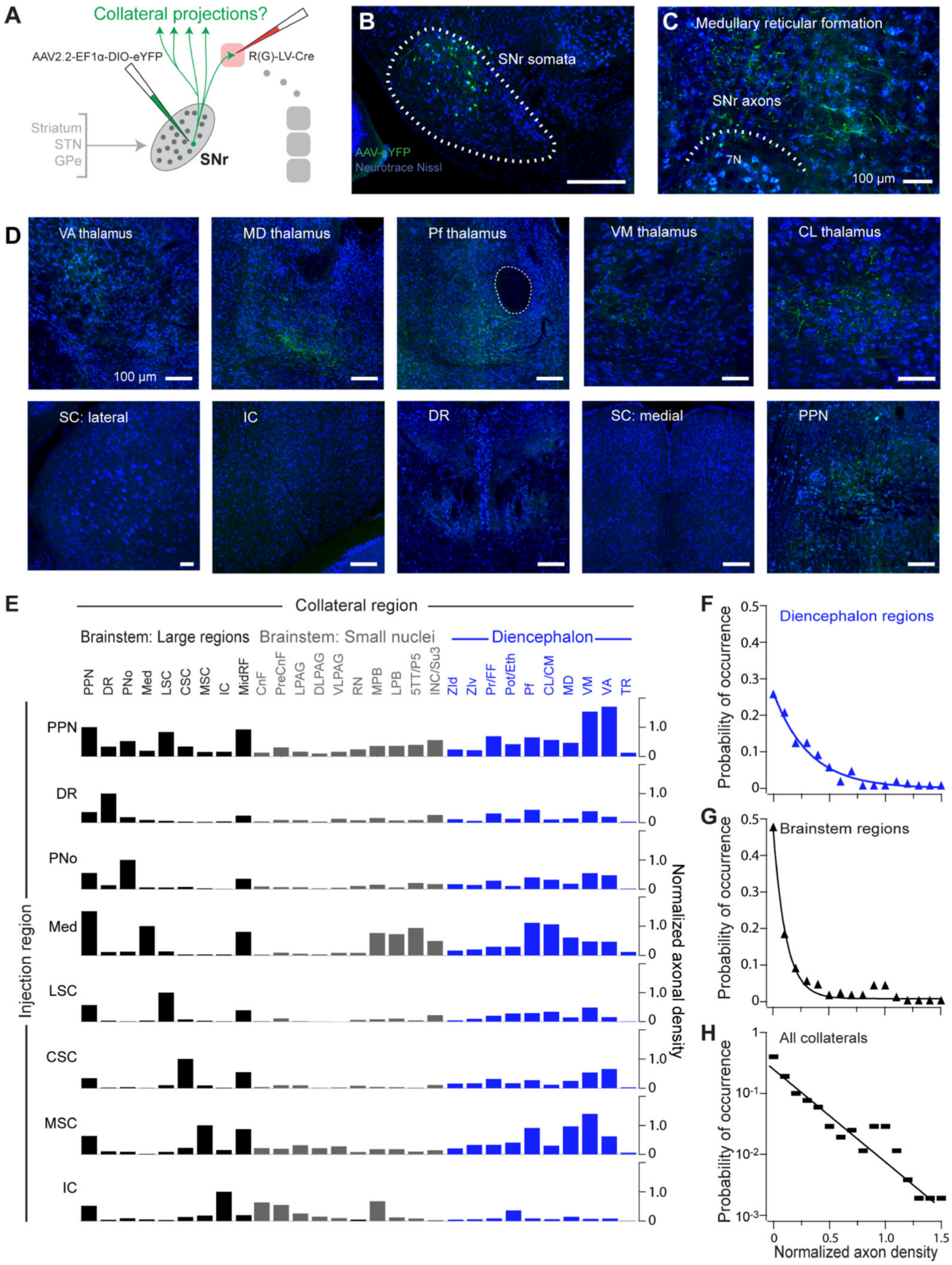

Figure 6. Broad and specific collateralization of SNr outputs demonstrated by projection-based intersectional viral mapping.

(A) Schematic of intersectional viral strategy to map SNr collateral projections across the whole brain. Injections of a retrograde lentivirus expressing Cre (RV(G)-LV-Cre) were made to a single downstream target. A Cre-dependent AAV expressing eYFP was injected into SNr, and the whole brain was serially sectioned and imaged for axon collaterals.

(B) Example injection site showing eYFP+ neurons in SNr following injections of retrograde Cre-expressing lentivirus into the medullary reticular formation and the Cre-dependent AAV expressing eYFP into SNr.

(C) Anterogradely labeled eYFP+ SNr axons at the lentivirus injection site in the medulla.

(D) Anterogradely labeled eYFP+ axon collaterals from SNr-medulla projecting neurons are distributed throughout diverse thalamic nuclei (top) and in the PPN (bottom right), but not in other large brainstem regions.

(E) Collateral projections from different SNr projection populations. Axonal density quantified in each downstream region (left-to-right) following labeling of specific SNr projection populations via injection of retrograde lentivirus expressing Cre to large brainstem regions (left) and AAV complementation in SNr. Axonal density normalized to that in the lentivirus-targeted region. See also Figure S7A.

(F) Compendium of collateral innervation density across diencephalic targets in all experiments.

(G) Compendium of collateral innervation density across brainstem targets.

(H) Occurrence of collateral innervation density across all targets; the line is an exponential with a decay constant of 0.27. See also Figure S7.

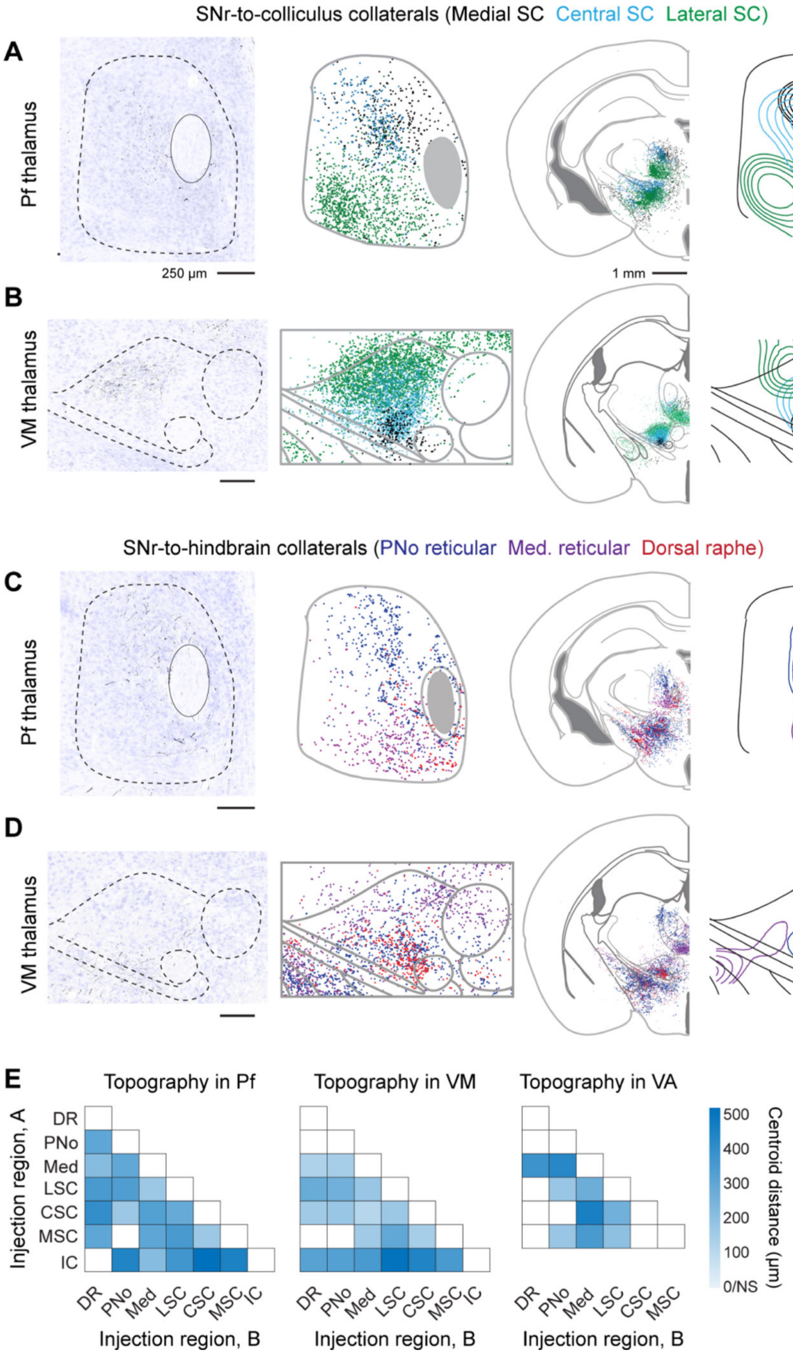

Figure 7. Parallel ascending collaterals target topographically distinct domains in intralaminar and motor thalamus.

(A, B) SNr neurons that project to the medial superior colliculus (black dots and contours), central superior colliculus (blue), and lateral superior colliculus (green) send collateral projections to parafascicular (Pf) (panel A) and ventromedial (VM) (panel B) thalamus. The left panels are single section examples of axon collaterals arising from neurons that project to the central (panel A) and lateral (panel B) superior colliculus. (Middle) composite overlay and (right) isodensity contour plots of collateral locations.

(C, D) SNr neurons that project to the hindbrain nuclei, including the pontine reticular formation (deep blue), medullary reticular formation (purple), and dorsal raphe nucleus (red) send collateral projections to Pf (panel C) and VM (panel D) thalamus. The left panels are single section examples of axon collaterals arising from neurons that project pontine reticular formation (panel C) and dorsal raphe nucleus (panel D). (Middle) composite overlay and (right) isodensity contour plots of collateral locations.

(E) Heatmap of Euclidean distances between centroids of collateral axon terminal fields in Pf, VM, and VA thalamus. Distances calculated pairwise for each collateral population labeled from SNr-brainstem targets, labeled ‘A’ and ‘B’. The intensity corresponds to the distance. White = not statistically different, $p < 0.01$. See also Figure S8.

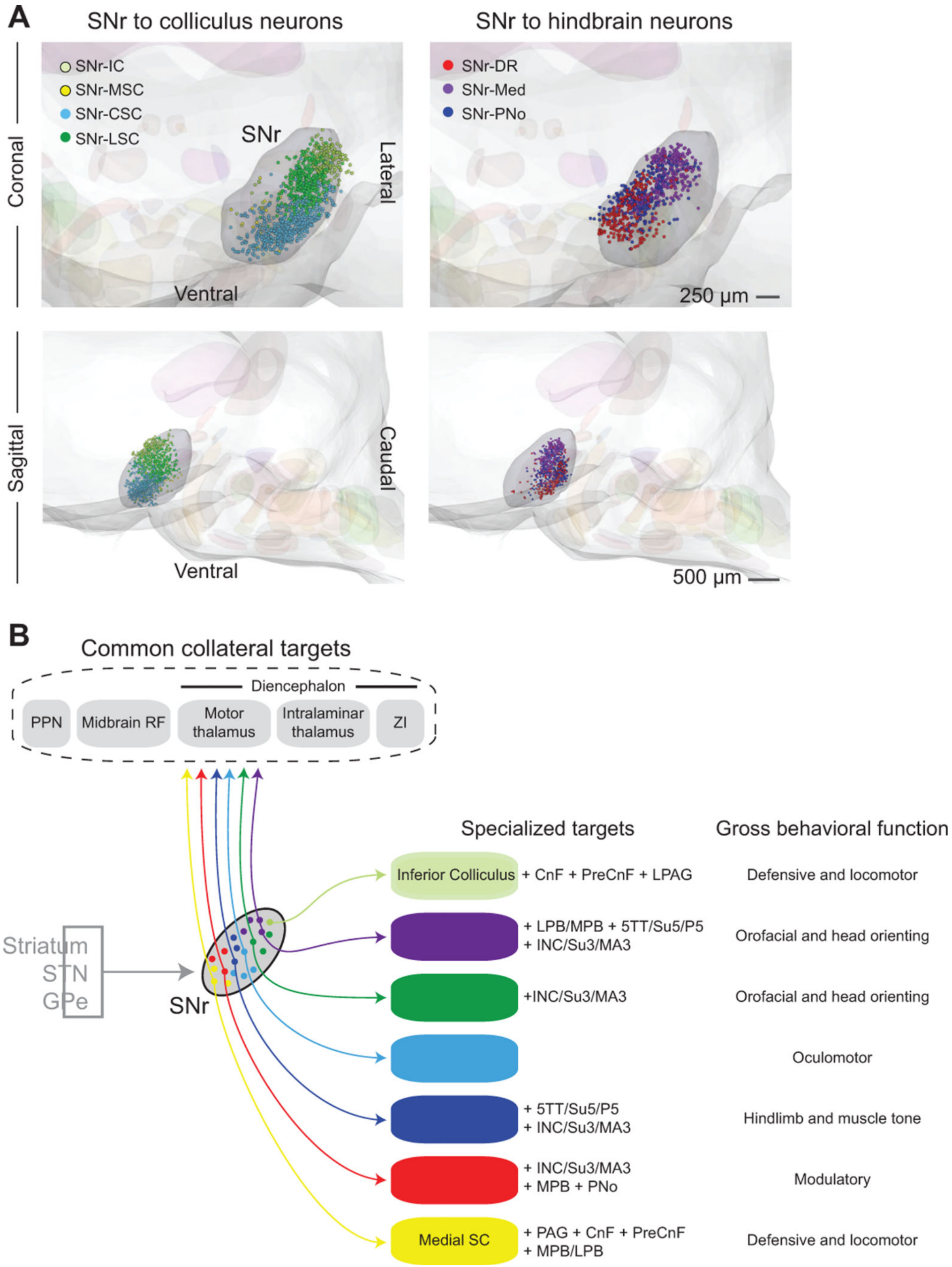

Figure 8. SNr subdivisions contain topographically organized projection populations.

(A) Three-dimensional reconstructions of SNr projection neurons labeled by retrograde viral tracers, aligned to a common brainstem atlas. The composite displays the relative position of SNr neurons projecting to midbrain (left) and hindbrain targets (right). Coronal (top) and sagittal (bottom) views of neurons projecting to the Inferior Colliculus (SNr-IC, light green), medial Superior Colliculus (SNr-MSC, yellow), central Superior Colliculus (SNr-CSC, light blue), lateral Superior Colliculus (SNr-LSC, green), Dorsal Raphe (SNr-DR, red), and PNo reticular formation (SNr-PNo, dark blue), and medullary reticular formation (SNr-Med, purple).

(B) Summary of SNr output pathways demonstrating unique and common targets of distinct SNr projection populations. Each SNr population projects to large, functionally-distinct brainstem regions and collateralizes to small brainstem nuclei and a set of common target regions. All projection populations demonstrate a distinct one-to-many projection pattern.

KEY RESOURCES TABLE

REAGENT or RESOURCE	**SOURCE**	**IDENTIFIER**
Antibodies		
Anti-GFP	Novus Biologicals	Cat#NB600–308; RRID:AB_10003058
Bacterial and Virus Strains		
AAV-DJ hSyn-FLEX-mGFP-2A-Synaptophysin-mRuby	Stanford Virus Core	Cat#GVVC-AAV-100
R(G)-lentivirus-hSyn-Cre	Wang Lab, MIT	Addgene plasmid #86641
AAV2/2-EF1α-DIO-EYFP	UNC Vector Core	N/A
R(G)-EIAV-DIO-FLP	Lim Lab, UCSD	N/A
AAV-DJ-EF1α-fDIO-EYFP	UNC Vector Core	N/A
Biological Samples		
Chemicals, Peptides, and Recombinant Proteins		
NeuroTrace™ 435/455 Blue Fluorescent Nissl Stain	ThermoFisher	Cat#N21479
Alexa 594-conjugated dextran	ThermoFisher	Cat#D22913
Kynurenic acid sodium salt	Abcam	Cat#ab120256
Picrotoxin	Abcam	Cat#ab120315
OPAL 520	Akoya Biosciences	Cat#FP1487001KT
OPAL 620	Akoya Biosciences	Cat#FP1495001KT
OPAL 690	Akoya Biosciences	Cat#FP1497001KT
Critical Commercial Assays		
RNAscope® Multiplex Fluorescent Reagent Kit v2	ACD	Cat#323100
Vectastain® Elite ABC-HRP Kit	Vector	Cat#PK-6100; RRID:AB_2336819
RNAscope® Probe -Mm-Pvalb	ACD	Cat#421931
RNAscope® Probe -Mm-Slc32a1-C2	ACD	Cat#319191-C2
RNAscope® Probe -Mm-Th-C3	ACD	Cat#317621-C3
RNAscope® Probe -Mm-Gad2-C3	ACD	Cat#439371-C3
Deposited Data		
Experimental Models: Cell Lines		
Experimental Models: Organisms/Strains		
B6.129P2-*Pvalb*$^{tm1(cre)Arbr}$/J	The Jackson Laboratory	Stock No. 017320; RRID:IMSR_JAX:017320
C57BL/6J	The Jackson Laboratory	Stock No: 000664; RRID:IMSR_JAX:000664
B6J.129S6(FVB)-*Slc32a1*$^{tm2(cre)Lowl}$/MwarJ	The Jackson Laboratory	Stock No: 028862; RRID:IMSR_JAX:028862

REAGENT or RESOURCE	**SOURCE**	**IDENTIFIER**
Oligonucleotides		
Recombinant DNA		
Software and Algorithms		
ImageJ	NIH	https://imagej.nih.gov; RRID:SCR_003070
MATLAB	MathWorks	https://www.mathworks.com/products/matlab.html; RRID:SCR_001622
Python, algorithms	Chen et al., 2019	https://github.com/mistycheney/MouseBrainAtlas; RRID:SCR_008394
VTK Visualization Toolkit		http://vtk.org; RRID:SCR_015013
Neurolucida	MBF Bioscience	https://www.mbfbioscience.com/neurolucida; RRID:SCR_001775
Igor Pro 6	Wavemetrics	https://www.wavemetrics.com/order/order_igordownloads6.htm; RRID:SCR_000325
ZEN Digital Imaging Blue 2.0	Carl Zeiss Microscopy GmbH	https://www.zeiss.com/microscopy/us/products/microscope-software/zen.html; RRID:SCR_013672
QuPath v0.2.1	Bankhead et al., 2017	https://qupath.github.io; RRID:SCR_018257
Other		
Axio Scan Z.1 Slide scanner microscope	Carl Zeiss Microscopy GmbH	N/A
ORCA-4.0 V3 digital CMOS camera	Hamamatsu	Cat# C13440–20CU
Sliding Microtome	Microm International	Cat #HM400
Nanoject II Auto-Nanoliter Injector	Drummond Scientific	Cat#3–000-204
Microinjector	Creative Instruments Development Company	N/A
Multiclamp 700B Microelectrode Amplifier	Molecular Devices	RRID:SCR_018455
ITC-18	HEKA	N/A
P-97 Flaming/Brown Micropipette Puller	Sutter	RRID:SCR_018636
DMZ Universal Electrode Puller	Zeitz-Instruments	RRID:SCR_014774
Vibratome VT1200S	Leica Biosystems	RRID:SCR_018453